University of Bologna "Alma Mater Studiorum", Naples "Federico II" and "Roma III", in convention with the "Istituto Nazionale di Geofisica e Vulcanologia"

Ph.D Thesis in Geophysics

XXIV Cycle

04/04 - GEO/10

Year 2012

Three dimensional seismic imaging and earthquake locations in a complex, segmented fault region in Southern Apennines (Italy)

Ph.D. Thesis of: *Ortensia Amoroso*

Coordinator	**Tutor**
Prof. Michele Dragoni	**Prof. Aldo Zollo**

Contents

Introduction

The southern Apennines of Italy is a seismically active belt characterized by a complex crustal environment in response of a very intense geodynamic activity. The area has been interested by large earthquakes both in historic and recent time. The last destructive earthquakes was the 23 November 1980, M 6.9, Irpinia earthquake which killed more than 3000 people and produced huge damage. Then a moderate magnitude earthquake (ML 4.9) occurred on 3 April 1996. The present day seismicity is characterized by small-to-moderate magnitude earthquakes (ML≤3.2). Although the present seismicity does not represent a real threat for the region and its inhabitants, it can be a useful probe for a deeper knowledge of the fault structures where the largest earthquakes occurred in the past.

In this framework, the present Thesis would be a contribution to improve the present day knowledge about seismicity location and the velocity model for the area. The Thesis has a twofold aim. First, benefiting from the recent installation in the area of a dense seismic network, that is, the Irpinia Seismic Network (ISNet), which allows the recording of microearthquakes, a 3D velocity model is retrieved for both P-wave and S-wave. Second, the three-dimensional image of the fault area based on a joint interpretation of the velocity models and the earthquakes location. To this aim two main directions have been followed. This first direction focused on one of the most critical aspects of data analysis concerning the optimal seismic phases identification. In this respect, a technique devoted to improve the S-phase identification has been developed which combines polarization analysis of single three components recording of a seis-

mic event with the analysis of lateral waveform coherence in a trace gathers (Amoroso et al., 2012). As a further improvement, a refined re-picking algorithm based on the waveforms similarity has been applied providing with a high-accurate observed travel-times dataset (Rowe et al., 2002). The second direction involved the adoption of a specific tomographic inversion strategy which allowed to infer more accurate velocity models and earthquakes location compared with those present in the literature. Specifically, an iterative, linearized, damped, tomographic approach (LeMeur et al., 1997, Latorre et al., 2004, Vanorio et al., 2005, Battaglia et al., 2008) has been implemented in which the arrival times of both P- and S-phase are simultaneously inverted for earthquakes location and velocities distribution estimation (Thurber, 1992). The inversion strategy is based on a multiscale approach (Bunks et al., 1995) consisting in a series of inversions with a progressively decreasing grid spacing. The Thesis is organized in four chapters. In the first chapter a description of the geological setting of the are under study is presented. The second chapter concerns the data selection criteria and the techniques adopted for the measurement of the seismic phases. The formulation of the inverse problem, the description of the tomographic inversion strategy are described in the third chapter. The fourth chapter contains the main results and the resolution analysis.

Chapter 1

Geological and structural setting of the Southern Apennines, Italy

1.1   Introduction

The Southern Apennines are one of the areas in Italy that are characterized by a very intense geodynamic activity. The formation of the Southern Apennines is related to westward subduction of the Apulian-Ionian lithosphere. Starting from the Upper Pliocene, the internal sector of the chain began to be affected by a NNW-SSE extensional tectonics (Doglioni et al., 1996). From the Upper Middle Pleistocene, a major change in the geodynamic evolution of the tectonic features triggered a phase of fast lifting which added an extension tectonic to the dominant NE-SW component (Westaway, 1993). The normal faults NW-SE oriented, parallel to the principal axis of the chain, developed in response to this extension (Valensise and Pantosti, 2001). As can be inferred from seismic catalogs, the Southern Apennines have been affected by several destructive earthquakes. In accordance with the extensional tectonics the fault plane solutions of these earthquakes, whose epicenters are confined within a narrow belt along the axis of the mountain chain, show predominantly normal

fault mechanisms in the NE-SW direction (Amato and Montone, 1997; Anzidei et al., 2001; Pasquale et al., 2009). In particular, the 23 November 1980 Ms 6.9 earthquake, was associated with a normal fault system consisting of three segments that were activated at three different instant of time (Bernard and Zollo, 1989). In this scenario, the analysis of background seismicity and three-dimensional crustal velocity models can help to improve understanding of the geometry of active faults and the recent tectonic evolution of the area.

1.2   Structure and regional geology

The structural architecture of the Southern Apennines is schematically described by a buried duplex system orogenically transported over the flexured southwestern margin of the Apulia foreland. The duplex system consists of the carbonate deriving from the Apulia Carbonate Platform (ACP) overlain by a pile of rootless nappes (Patacca and Scandone, 1987). The ACP consists of 78 km thick Mesocenozoic carbonate sequence, which overlies Permotriassic clastic deposits (Verrucano Fm., Roure et al., 1991). PlioPleistocene terrigenous deposits stratigraphically cover the flexed ACP in the eastern margin of the Bradano Trough (Casnadei, 1998). Moving westward to the external zone of the belt, the ACP progressively dips below the rootless nappes and is in turn involved in the folds and thrusts of the thrust belt (Figure 1.1).

The thrust sheet stacks overlying the ACP are derived from the deformation of three main palegeographic domains (Patacca et al., 1992):

- the Lagonegro Basin located between the Apulia Carbonate Platform and the Western Carbonate Platforms;

- the Western Carbonate Platforms, consisting of Mesozoic and Paleogene carbonate sequences followed by Upper Miocene siliciclastic flysch deposits;

- internal basin domains, which are related to the Sannio and Sicilide Com-
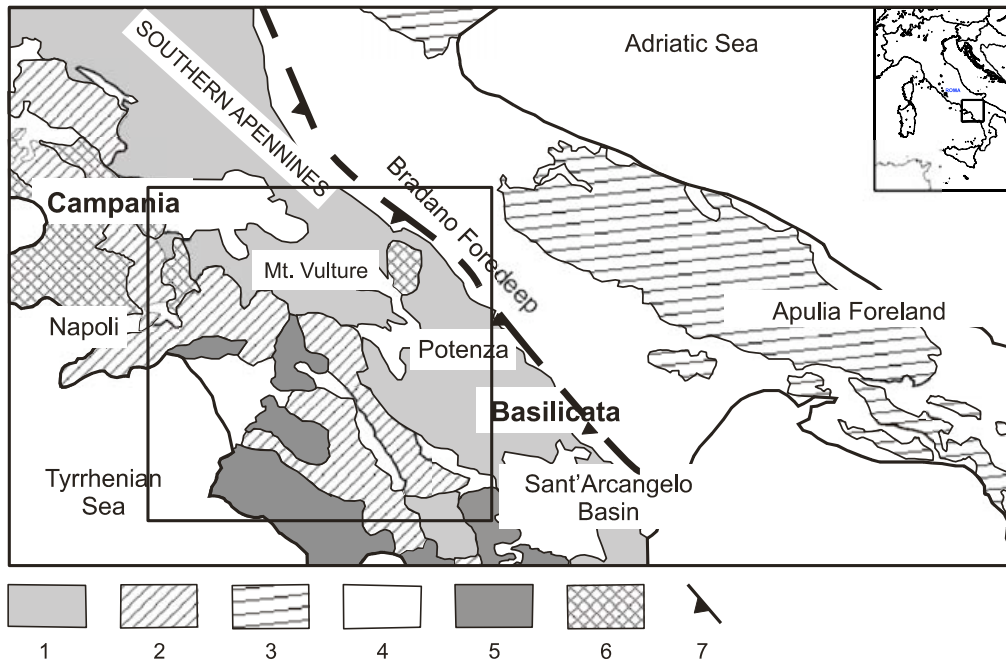
Figure 1.1:   Simplified geological map of the southern Apennines showing the major structural features (DeMatteis et al., 2010). 1. Molise - Sannio - Lagonegro pelagic basin and related foredeep deposits; 2. Apennine carbonate platform; 3. Apulia carbonate platform (ACP); 4. Pliocene - Quaternary terrigenous deposits; 5. Ligurides and Sicilides; 6. Magmatic units; 7 Main thrust front.

   plexes.

Syntectonic terrigenous sequences do not uniformly cover the thrust sheet stacks and represent the infill of satellite basins of Late Tortonian to Early Pleistocene age (Patacca and Scandone, 2001).

In additional to geological analysis our present knowledge of the upper crustal structure has benefited from intense hydrocarbon exploration. Thanks to industrial seismic reflection survey and well data collected in the area the deep structure of the Southern Appenines is well reconstructed to a depth of about 10 km (Mostardini and Merlini, 1986; Patacca and Scandone, 1989; Casero et al., 1991; Roure et al., 1991; Menardi and Rea, 2000; Scrocca et al., 2005). Moreover, recent cross section interpretation of the seismic reflection profile

CROP04, shown in Figure 1.2, (Cippitelli, 2007) allowed the identification of: the top of the Apennine Platform; the top of Lagonegro-Irpinia flysch sequence or imbricate; the top of Apulia Platform carbonate and the base of carbonate sequence (Figure 1.3).

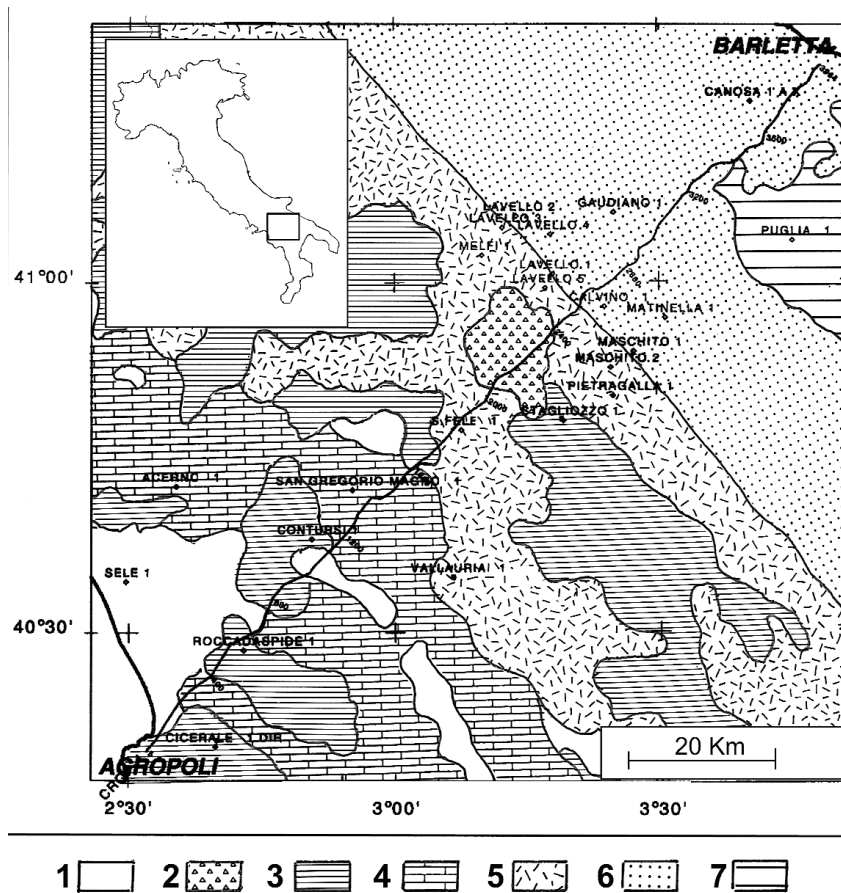Figure 1.2:   Schematic structural map showing the layout of the CROP04 seismic profile together with the location of the most important exploration wells drilled in the study area (Cippitelli, 2007): 1) alluvial-pyroclastic Olocene sediments; 2) Vulture volcanics; 3) Liguride-Sicilide-Cilento flysch; 4) Apennine Platform; 5) Lagonegro and Irpinia flysch imbricates; 6) Bradano Plio-Quaternary overburden; 7) Outer Apulia Platform.
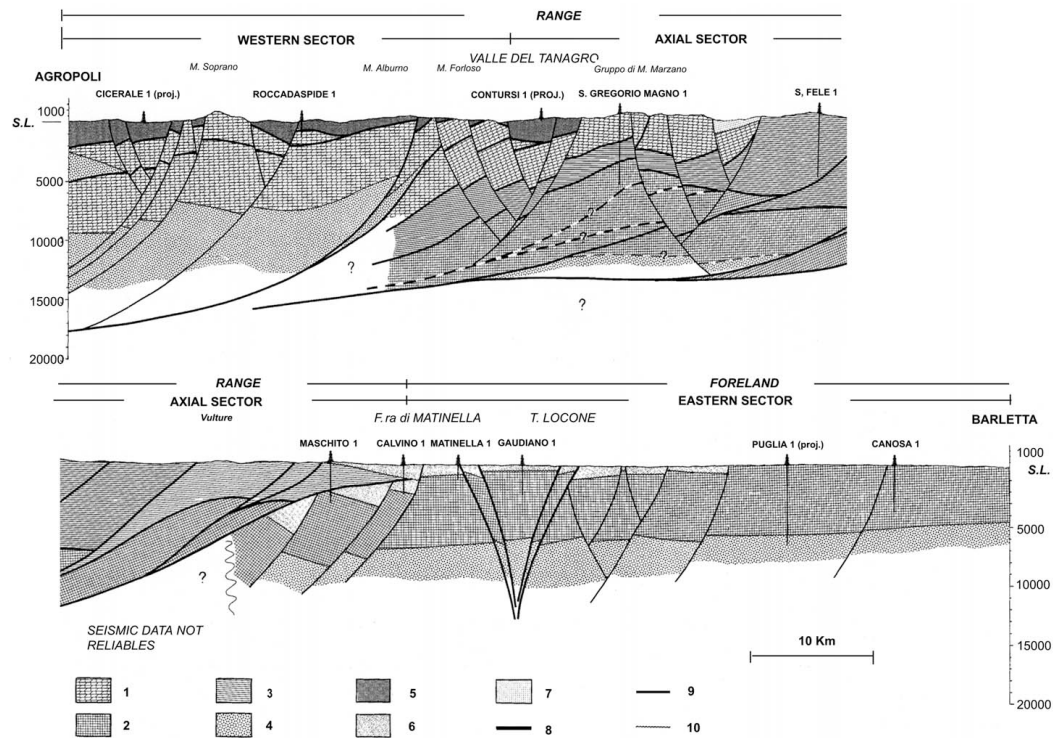
Figure 1.3: Structural cross-section Agropoli-Barletta inferred from the depth conversion of the two-way time structural features recognized from the CROP04 seismic profile interpretation (Cippitelli, 2007). 1) Apennine Platform 2) Apulian Platform 3) Lagonegro and Irpinia flysch 4) Permo-triassic substratum 5) Cilento Flysch and Liguride-Sicilide complex 6) Plio-Quaternary everburden 7) Castelgrande Sandstone 8) reverse fault-overthrust plane 9) normal fault 10) unconformity.

1.3 Seismicity

The southern Apennines have been experienced several destructive earthquakes both in historic and recent times. Figure 1.4 shows the locations and the dates of the most know earthquake as reported in CSI catalogue.

The 23 November 1980 Ms 6.9 Irpinia earthquake

The most recent destructive event is the 23 November, 1980, Ms 6.9 earthquake. This earthquake was characterized by three distinct rupture episode,
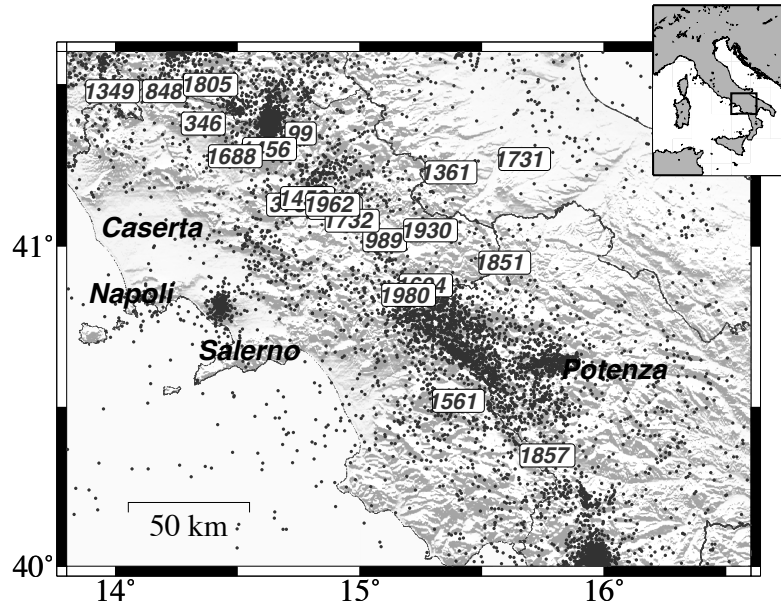
Figure 1.4:   Map of the instrumental seismicity of southern Apennines (period 1981-2008, from the CSI catalog, see http://csi.rm.ingv.it). Dates of historical earthquakes with magnitude larger than 6.0 are reported.

occurred at 0s, 18s and 39s, associated with normal faulting. The three segments together with their corresponding seismic moment and the beach balls are shown in Figure 1.5. The first episode ruptured two faults striking northwest before triggering the failure of an isolated fault in the north, with an uncostrained mechanism, different from the earlier one (Bernard and Zollo, 1989). The Monte Marzano segment ruptured first and the associated fault showed a normal mechanism on a plane dipping 60° toward the northeast (Fig. 1.5). The Monte Picentini segment ruptured from its southern edge about 2s afterward, with the same mechanism and with a length of 20 km. The second episode consisted in the rupture of the southern segment occurring on a low dip-angle normal fault (20°) asssociated with secondary shallower faults with a length of 20 km. The last episode at 40s may have activated a fault plane antithetic to the Monte Marzano segment (Fig. 1.5). This inusual pattern of

faulting is a consequence of the complex structural geology characterizing the tectonic environment in which the fault system is embedded.

Since 1980, the largest event that occurred within the epicentral area of the 1980 earthquake was the 3 April 1996 ML=4.9 earthquake, which characterized by a normal faulting mechanism (Cocco et al., 1999).
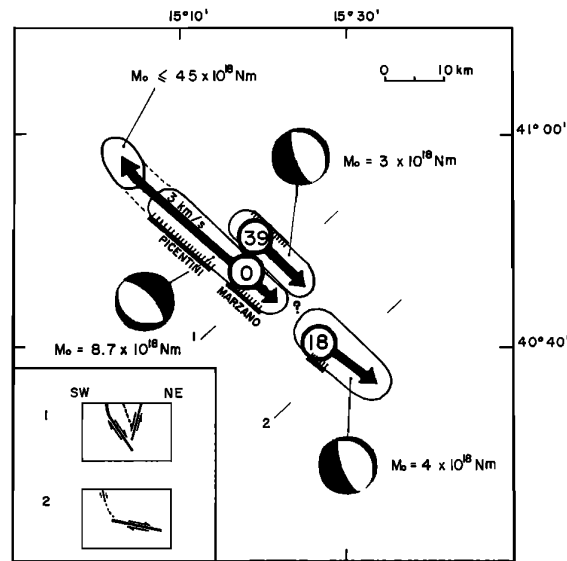
Figure 1.5: Sketch of the rupture process and associated mechanism for the Irpinia, November 23, 1980 earthquake (Bernard and Zollo, 1989).

The 5 May 1990 Ml 5.2 and 26 May 1991 mb 5.1 earthquakes

Ten years after the 23 November 1980 Irpinia Ms 6.9 earthquake, a moderate event on 5 May 1990 $M_L = 5.2$ occurred approximately 40 km east of the southern end of the 1980 aftershock zone causing damage in the nearby town of Potenza. Approximately one year later, the 26 May 1991 $m_b = 5.1$ earthquake struck the same area, causing additional minor damage in the Potenza area. Both the two earthquakes were characterized by strike-slip faulting on an oriented plane approximately east-west (DiLuccio et al., 2005).

Present-day background seismicity

The present-day micro-earthquakes distribution is characterized by event with moment magnitude ranging between 0.9 and 3.2, and mainly occurs on the NW-SE striking normal fault system along the Apenninic belt and on a nearly E-W alignment in the Potenza region which transversely cuts the chain (De-Matteis et al., 2012). The depth distribution is located in the uppermost 15 km of the crust except in the Potenza region where the earthquake can be occur at larger depth (25 km).

1.4 Tomographic images of the Southern Apennines: status at present

The velocity models currently available in literature for the area under study provide substantial information about the P wave velocity structure on a wide scale. In the present section the most important papers and findings are reported:

- Amato et al. (1992) and Amato and Selvaggi (1993) have imaged the three-dimensional velocity structure in the epicentral area of the 23 November 1980 earthquake, using Thurber's inversion technique for both hypocenter and velocity parameters. The used dataset consisted of the both aftershocks recorded by a local network temporarily installed in the area. Their results show that the main rupture occurred along a sharp NW-SE trending velocity, due to a crustal discontinuities (Figure 1.6). The velocity variation along the fault reflects the complex feature of the earthquake. The analyzed seismicity is concentrated beneath the Marzano-Valva sub-segment, where the maximum slip was observed. The region of the Sele Valley, where no surface slip was observed, is characterized by strong low velocities in coincidence of a lack of seismicity in the upper 7 km (Figure 1.7);
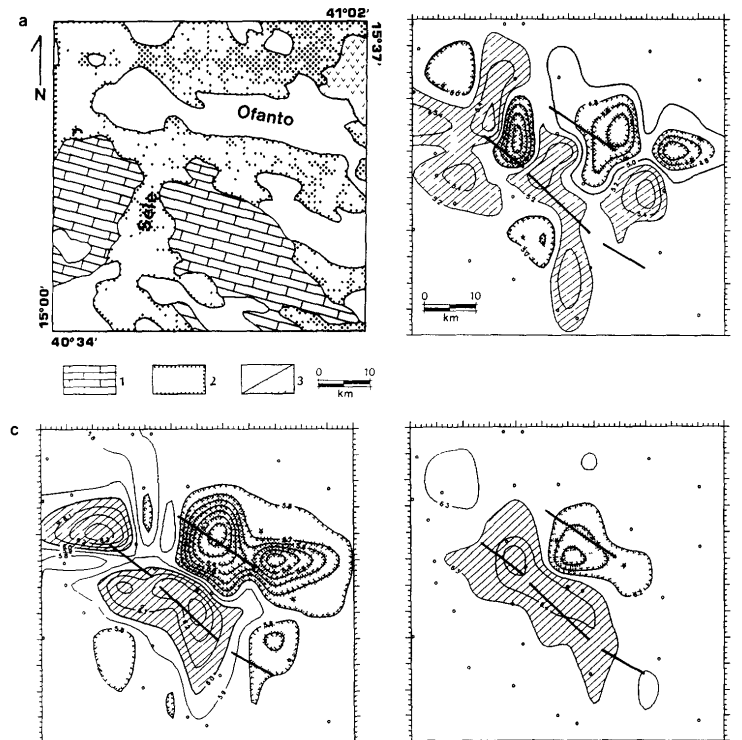
Figure 1.6: (a) Simplified geological map of the Irpinia region, (b), (c), (d) P velocity anomalies at 3,6 and 9 km depth, respectively. The dashed area corresponding to the high velocity, the dotted sones are low velocity (Amato et al., 1992).

- Chiarabba and Amato (1994) discussed the relationship between the seismogenic behaviour of the faults and the velocity structure of the area as inferred from seismic tomography. In particular, they interpreted the high velocity zones as a brittle region with high-strength rock and the low-velocity zones as a region where weak material are prevalent. Their findings suggested that large lithological and rheological heterogeneities in the shallow crust played a crucial role in the rupture process of the Irpinia earthquake.

- Improta et al. (2003) analyzing and interpreting gravimetric data, seismic reflection and information from deep wells, retrieved information on the upper crustal structure in the Irpinia region. In particular, they
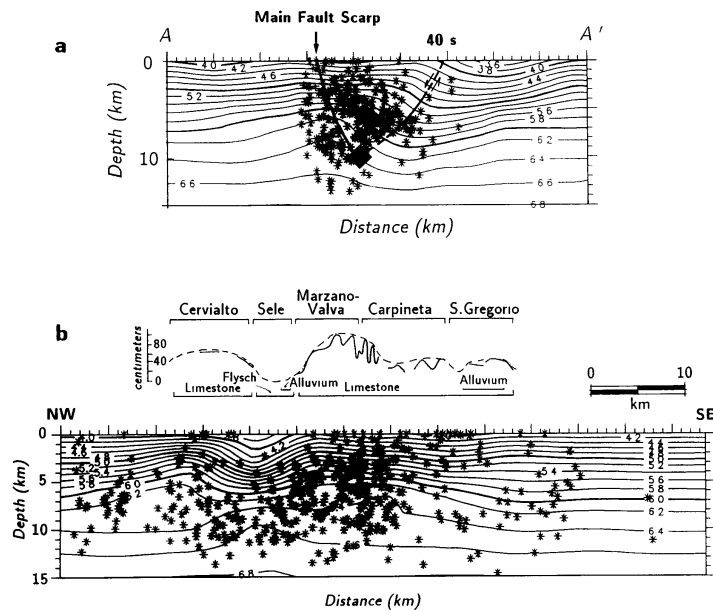
Figure 1.7:   (a) Cross-section perpendicular to the main fault. (b) Cross-section parallel to the main fault (Amato et al., 1992).

found that a) the velocity structure in the upper crust is strongly in-fluenced by the geometry of the ACP, whose structural lows and highs give rise to pronunced low- and high-velocity anomalies, respectively b) a relationship between ACP geometry and the 23 Novembre 1980 Ms 6.9 Irpinia earthquake c) correlation between P-wave velocity and sedimentary rocks composing the Apennines crust (see the table in Figure 1.8)

- In a recent work, DeMatteis et al., 2010 propose a 3D P-waves velocity model retrieved from the inversion of the catalog data from 1988 through 2004. The tomographic images show the presence of a high-velocity zone correlated with the Apennine and Apulia carbonatic platforms, while the low velocities body are associated with basinal deposits. The distribution of relocated seismicity in the obtained 3D velocity model, shows that the largest part of the seismicity is well correlated with the faults of the 1980 Irpinia earthquake. This evidence strongly supports the need

Table 1

Tectono-stratigrafic units	Prevalent lithology	Density range (g/cm3)	P-wave velocity range (km/s)
Apulia carbonate platform	limestones, dolomites, anhydrites	2.7	6.0−6.5
Western carbonate platform	limestones, dolomites	2.60−2.65	5.3−6.0
Lagonegro Basin (Mesozoic)	radiolarites, cherty limestones, dolomites, siltstones	2.55−2.60	4.4−6.2
	siliceous claystones (Galestri Fm.)	2.5	3.5−4.4
Cenozoic basinal successions (Lagonegro Basin, Silicide and Sannio complexes)	variegated clays, shales	2.35	2.8−4.2
	siliciclastic flysch deposits (Upper Miocene)	2.45	3.3−4.4
	calcareous and arenaceous turbidites	2.45−2.50	4.0−5.2
Thrust sheet−top clastic sequences (Pliocene−Early Pleistocene)	clays, sandstones, conglomerates	2.25	2.0−2.4

Figure 1.8: P wave velocities for Southern Apennines Rocks (Improta et al., 2003).

to investigate the properties of the fractured zone on a local scale in relation to the potential reactivation during future large earthquakes.

Vp/Vs ratio

The V_p/V_s ratio can be associated with the elastic characteristics of rock under investigation and with the physic state of the pore fluid. The available information on the V_p/V_s ratio for the area under study provide a single value for the whole area. It has been found by optimizing the value of RMS residual of 1D and 3D localization patterns. The proposed values indicate that this ratio is greater than or equal to 1.8 (Maggi et al., 2009; Deschamps and King, 1984; DeMatteis et al., 2010, DeMatteis et al., 2011). The relatively high V_P/V_S ratio value could be related to the presence of highly fractured zones characterized by the presence of fluids.

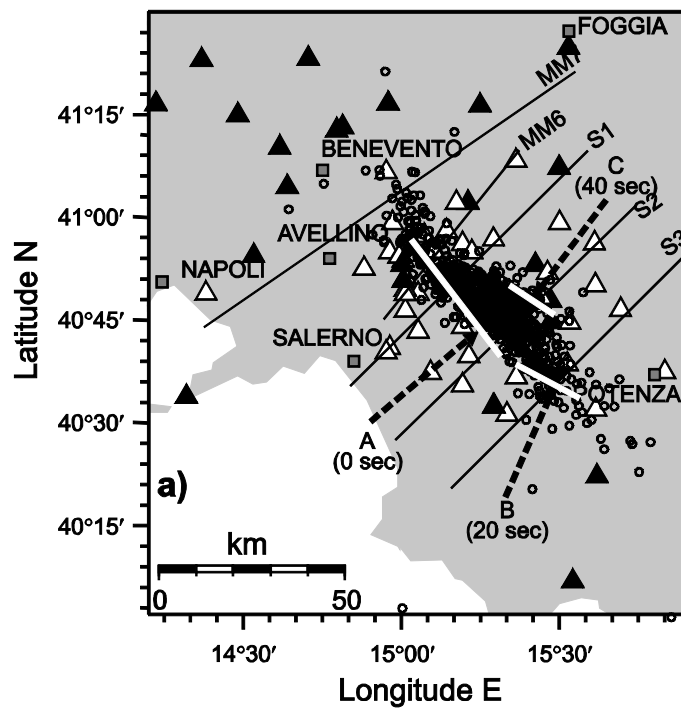Figure 1.9:   Epicentral distribution of the aftershocks of the Irpinia earthquake located in the 3D tomographic model retrieved by DeMatteis et al. (2010). MM6 and MM7 indicate the vertical sections shown in Figure 1.10
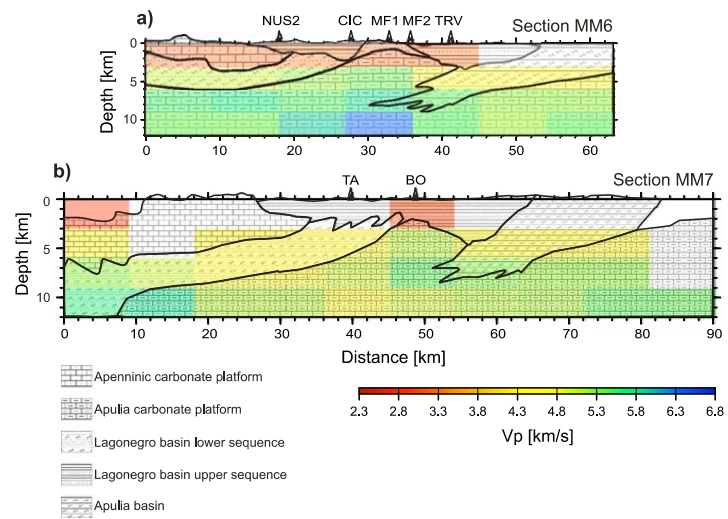
Figure 1.10: P wave tomographic cross-section (DeMatteis et al., 2010) superimposed on the MM6(a) and MM7(b) sections of Mostardini and Merlini 1986 (see figure 1.9 for the sections direction).

Chapter 2

Data and processing technique

2.1 Introduction

High-resolution imaging with microseismic events requires the use of large and consistent data sets of seismic phase arrival times. The common procedure of reading the arrival time of a phase (*picking*) involves the manual measuring of P-and S arrivals on recordings of a single event at a time. Systematic errors can be introduced due to inadequate working procedures such as: the interaction between the process of picking and the result of the location, which can lead the operator to shift the pick to reduce the standard deviation of the residuals (RMS) calculated for the location, when the picking activity is shared by many operators, or when data have been collected at different networks. The inconsistency of the data can remain unnoticed when the data are used to analyze the events independently from each other, but may clearly appear when performing studies of joint determination of the hypocentral parameters and velocity model. The only way to reduce the inconsistency is to completely revise the picking. However, the growing number of dense seismic monitoring networks installed in areas of high seismicity offers a continuously increasing availability of high-quality three-component recordings (3C) which has motivated the study of techniques for automatic picking. The approaches to automatic picking can be divided into main categories. The first one is to

analyzes a single event at a time doing the picking on each seismogram independently from the others. In this context, traditional methods quantify some attributes of waveforms such ad amplitude, frequency content or polarization in a characteristic function, and apply the automatic detection of the phase directly to this function (Allen, 1978, Diehl et al., 2009). Other methods, such as neural networks, working directly on the seismograms avoiding the need to calculate attributes or characteristic functions (Dai and MacBeth, 1997). A second approach works on several seismograms at once, exploiting the similarity of waveforms from nearby events (Rowe et al., 2002) inheriting, in some cases, from the passive seismic technique the collection of the traces in sections (Amoroso et al., 2012). The single-trace approach is more suitable for real-time analysis because it is not based on restrictive criterion of similarity of waveforms (Lomax et al., 2002; Vassallo et al., 2002). On the other hand, the multi-trace approach is inherently more suitable for studies of relatively small volumes such as those in which events tend to clusterize (Rowe et al., 2002).

In this chapter I describe the used dataset, the selection made based on the quality of the localization, the technique developed and adopted for the correct identification of S-phase, and the approach followed for the refined re-picking P and S.

2.2   Network and data selection

The dataset analyzed consists of 1312 events with local magnitude $0.1 \leq$ Ml ≤ 3.2, recorded by 26 stations of the Irpinia Seismic Network (ISNet) and 16 stations of the network Istituto Nazionale di Geofisica e Vulcanologia (INGV) in the period August 2005 through April 2011 (Figure 2.1). The P- and S-phases were initially read manually on 3C ground velocity recordings. The seismic events were located in the 1D reference velocity model for the area (DeMatteis et al., 2011), by using the NLLoc code (Lomax et al., 2000). Figure 2.2 shows the distribution of the main earthquake location parameters. It can

be noted that the mean horizontal error location is about 1.4 km while the vertical error is about 1.5 km.
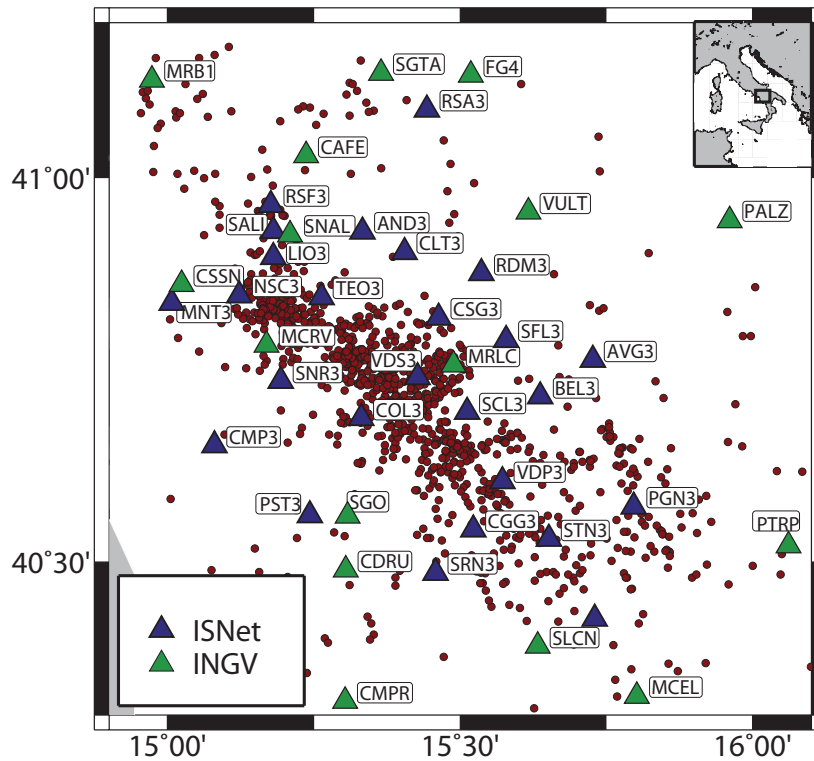
Figure 2.1:   Epicentral distribution of the analyzed seismic events (red dots) recorded by ISNet (blue triangles) and INGV stations (green triangles) in August 2005 through April 2011.

A first selection of the whole dataset was performed on the basis of the location quality: only the events that have at least 5 P- and 2 S- picked arrival times, an azimuthal gaps lower than 200 degrees and RMS of location lower then 0.5 s have been selected. The selection reduced the event from 1312 to 634.

In the analyzed dataset it was observed that similar event, recorded at the same station, shows inconsistency P- and S-phases picking. This inconsistency may be due to changes in the signal to noise ratio or to the presence of multiple arrivals (due to the phenomena of conversion or multi-path) producing
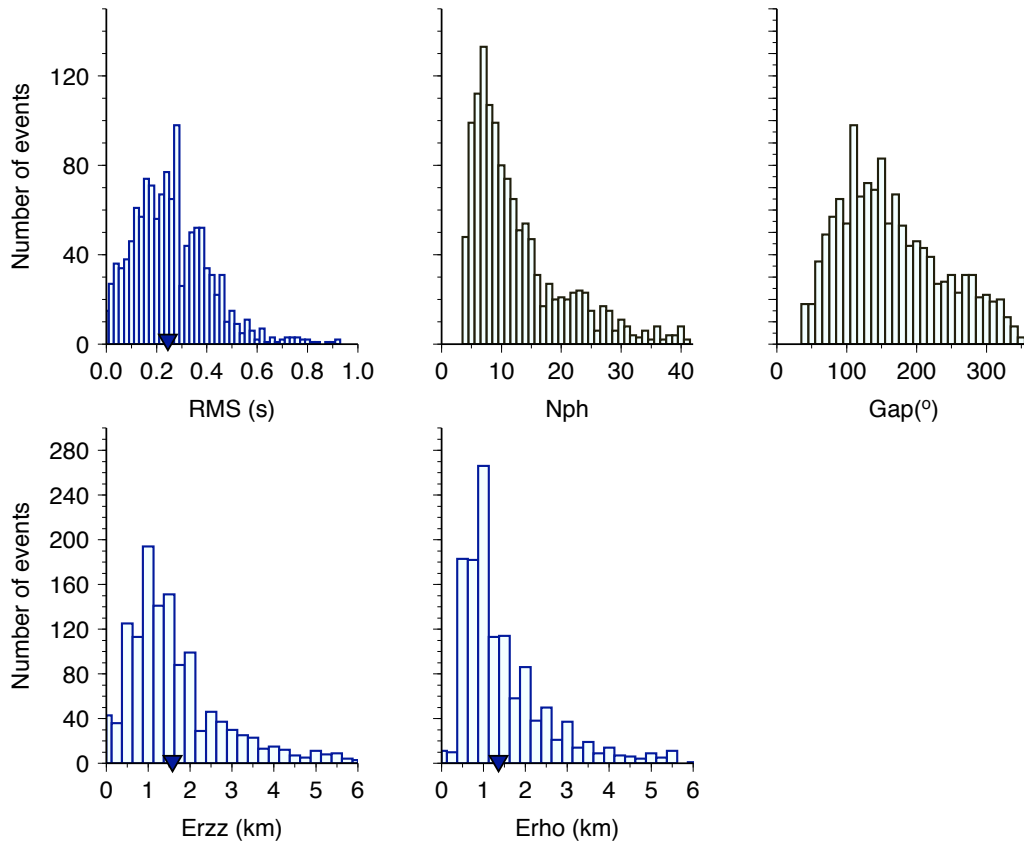
Figure 2.2:   Parameters which provide information on the reliability of the earth-
quakes location. RMS : root mean square travel time residuals. Nph: number of P
and S arrival-time observations used to compute the hypocenter location. Gap: the
largest azimuthal gap between azimuthally adjacent stations. Erho: the horizontal
location error defined as the length of the largest projection of the three principal
errors on a horizontal plane. Erzz: the depth error defined as the largest projection
of the three principal errors on a vertical line.

uncertainties in hypocentral location or distribution of wave velocities in the subsurface. In the next section the technique for the correct identification if S-phase developed in the present thesis is introduced.

2.3 S-wave identification by polarization filtering and waveform coherence analyses

Usually the S-waves are identified on one of the horizontal components of a seismogram through the variation in amplitude and frequency of the signal with respect to the preceding P-waves. The correct reading of the arrival times of these waves can be complicated by various factors, such as the superposition of the tail of the P-wave, the presence of converted waves generated at different interfaces, and the splitting of S-waves caused by seismic velocity anisotropy (Crampin, 1977). These factors often can have such large influences that an operator can make significant errors in phase identification or even abandon the reading of these waves.

In passive seismic studies, this problem is approached independently for every single station, using different multicomponent filters applied to the individual three-component records. These filters exploit the main characteristics of the S-waves, such as, for example, their linear polarization and the perpendicular direction of the particle motion of the S-waves with respect to those of the P-waves (Vidale, 1986; Montalbetti and Kanasewich, 1970; Kanasewich, 1981; Flinn, 1965). A characteristic function can be defined that, once cleaned of the P-waves, clearly reveals the S-wave arrivals (Cichowicz, 1993). Recently, Diehl et al., 2009 integrated this approach with automatic conventional detection and picking techniques, to obtain in-situ estimations of the uncertainty and of the quality of the corresponding waves recorded.

Lateral waveform coherence and the slowness of an arriving wave can be determined with recordings from several stations, as it is done in array seismology (Rost and Thomas, 2002). Moreover, processing methods in active exploration seismics typically employ many records from different stations and

sources simultaneously. Depending on the source and receiver geometry, traces are grouped in various types of gathers, and move-out and stacking techniques can be applied to enhance desired phases in these seismic sections (e.g. Ylmaz, 1987). The sum of the traces (stack trace) improves the coherent signal along the chosen move-out curve, while reducing random noise and the amplitudes of other, undesired phases appearing with a different slope in the seismic section. In the present study, we propose a new data processing technique that aims at an unequivocal identification of S-wave arrival times using the recordings from all stations of a seismic network. In particular, the technique combines polarization analysis of single three-component recording of an event with the analysis of lateral waveform coherence in trace gathers. The proposed procedure provides seismic sections in which the first arrivals are the S-waves. In a novel approach the average S-wave velocity in the study area is measured from these sections by a stacking velocity analysis similar to the techniques used in exploration seismics. The efficacy of the technique is evaluated with synthetic seismograms.

2.3.1 Method

The followed methodological approach can be outlined in the following way:

- P-wave picking and initial localization of the event and subsequent trace rotation;

- Polarization filtering and construction of a characteristic function CF_{SW} for S waves;

- Gathering of the CF_{SW} function traces in sections;

- Linear move-out and stacking velocity analysis.

First, to separate the P-wave energy from the SV and SH components, the three-component records are rotated from the laboratory reference system defined by the vertical component (Z), the north-south component (N) and the

east-west component (E) into the ray-coordinate system defined by L, Q and T. The L component represents the main direction of the particle motion of the P-waves, the T component represents the transversal particle motion (the SH energy), and the Q component represents the normal vector for both L and T (the SV energy). The rotation is achieved using the incidence angle ϕ and the backazimuth β of the first P-wave and the following rotation matrix (Plesinger et al., 1986):

$$\begin{pmatrix} L \\ Q \\ T \end{pmatrix} = \begin{pmatrix} cos\phi & -sin\phi sin\beta & -sin\phi cos\beta \\ sin\phi & cos\phi sin\beta & cos\phi cos\beta \\ 0 & -cos\beta & sin\beta \end{pmatrix} \cdot \begin{pmatrix} Z \\ E \\ N \end{pmatrix} \quad (2.1)$$

Here the backazimuth β is determined from the epicenter location relative to the analyzed station. The incidence angle ϕ is measured in a short (0.3 s) time window starting at the P-wave pick using polarization analysis based on the three-component covariance matrix (Montalbetti and Kanasewich, 1970). After rotation into the ray coordinate system, several polarization attributes are calculated in a moving time window to identify and enhance the S-wave signals on the rotated seismograms. In order to choose the optimal window length for the covariance matrix, Cichowicz, 1993 suggest it can be estimated from the predominat frequency. For this purpose we use the parameter

$$\tau_c = \frac{2\pi}{\sqrt{\int_0^{t_0} \dot{u}^2 dt / \int_0^{t_0} u^2 dt}} \quad (2.2)$$

introduced by Kanamori, 2005 which is a good estimator for the predominant period of the signal having the advantage to be measured in time domain. In Eq. (2), $\dot{u}$ and u are the velocity and the displacement, respectively, while in the following applications t_0 is set to $3s$.

The polarization attributes are computed from the eigenvalues and the eigenvectors of the covariance matrix. Particularly useful for S-wave detection are the directivity $D(t)$, the rectilinearity $P(t)$ and the ratio between the transverse energy and the total energy $H(t)$. The directivity $D(t)$ is defined as the angle normalized to 1 between the L and the eigenvector corresponding to the

maximum eigenvalue of the covariance matrix. Because the S-wave polarization is perpendicular to the P-waves, the directivity is 0 for the first P-wave arrival and approaches 1 for the first S-wave arrival. To utilize the linear polarization of S-waves a measure of the level of linear polarization is calculated. According to Samson, 2002 this rectilinearity $P(t)$ it is given by:

$$P(t) = \frac{(\lambda_1 - \lambda_2)^2 + (\lambda_1 - \lambda_3)^2 + (\lambda_2 - \lambda_3)^2}{2(\lambda_1 + \lambda_2 + \lambda_3)} \tag{2.3}$$

where $\lambda_1 \lambda_2 \lambda_3$ are the eigenvalues of the covariance matrix at time t, sorted in decreasing order. $P(t)$ has values near 0 for the elliptical or undetermined polarization states, and it reaches a value equal to 1 when the polarization is perfectly linear, as expected for the first arrivals of both the P-waves and S-waves. The ratio between the estimated energy on the transverse component and the total energy is:

$$H(t) = \frac{\sum_j Q_j^2 + t_j^2}{\sum_j L_j^2 + Q_j^2 + t_j^2} \tag{2.4}$$

Also this operator is taken as tending to 1 for the first S-wave arrivals and to 0 for the first P-wave arrivals. Finally, as originally proposed by Cichowicz (1993), the product of the squares of the three operators $D(t)$, $P(t)$ and $H(t)$ give the characteristic function for the detection of the S-waves:

$$CF_S = D^2(t) \cdot P^2(t) \cdot H^2)(t) \tag{2.5}$$

In general, this characteristic function alone does not always allow an unequivocal identification of the S-wave arrivals because it depends on the assumption that the angle of incidence can be calculated accurately from the analysis of the polarization of the incident P-waves, and that the S-waves are linearly polarized. In many cases, it can be advantageous to include amplitude information in the form of a weights. As a weight function we propose the square root of the sum of the squares of the transversal components:

$$W(t) = \sqrt{Q^2(t) + T^2(t)} \tag{2.6}$$

To illustrate the three-component processing, Figure 2.3 shows the original and rotated traces of a synthetic three-component seismogram together with the computed polarization attribute traces D, P and H , and the weighted characteristic function CF_{sw} . The first P-wave arrival is at 0.0 s and the S-wave arrival at about 3.4 s, the polarization window length is set to 0.25 s. It can be seen that in correspondence with the S-wave there are simultaneous increases in the functions D, P and H. These are also reflected in the absolute maximum of the characteristic function CF_{sw} (Fig. 2.3a, bottom trace), which prominently marks the first S-wave arrival.

The polarization analysis produces only one time series CF_{sw}, that summarizes the polarization characteristics of S-waves measured from a three-component recording of an event. To make the S-wave identification more robust, lateral waveform coherence and the apparent velocity of a given phase is analyzed in gathers of traces. Useful gathers are common receiver gathers (CRGs), in which the recordings of one single station are combined, or common source gathers (CSGs) in the case of recordings of the same source. In contrast to conventional gathers used in exploration seismics, here the traces in each section are sorted by hypocentral distance instead of the epicentral distance (offset), because of the distribution of the earthquakes in depth. In a section sorted by hypocentral distance, different types of seismic waves can be distinguished by their different slopes, i.e. their different apparent velocities.As an example, Figure 2.3b shows a synthetic CSG section of traces reduced at (bottom) and the corresponding stack trace (top). The synthetic records were created with AXITRA (Bouchon and Aki, 1997, Cotton and Coutant, 1997) for a local earthquake on May 27, 2008, 16:19:33 UTC, recorded at ISNet stations. The one-dimensional velocity model of Amato and Selvaggi, 1993 was used, and noise had been added to the seismograms before computing the traces. Due to the applied reduction velocity, the first S-wave arrival aligns near 0.0 s. The stack trace clearly indicates the S-wave arrival, while energy visible at earlier or later times on individual traces are suppressed in the stack. The time shift of 0.1 s observed for all the traces shown in 2.3b can be attributed to the finite
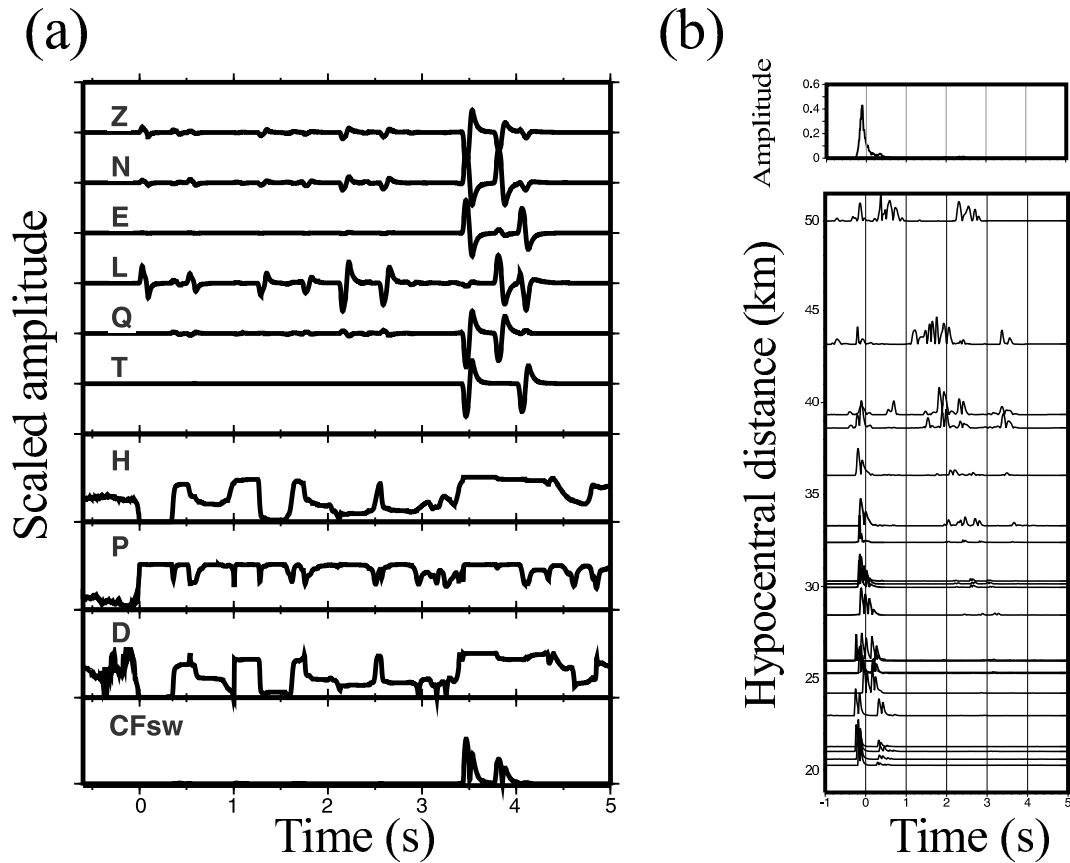
Figure 2.3:   (a) Synthetic seismogram example of the three-component processing. Z, N, E are the original and L, Q, T are the rotated components. H, P, D are the polarization attributes, and CF_{sw} is the weighted characteristic function. The first P-wave arrival is at 0.0 s, and the direct S-wave arrives at about 3.4 s. (b) Common source gather (CSG) of the CF_{sw} traces from a single, simulated event recorded at different station. The S-wave arrivals are aligned near 0.0 s, and the top trace is the stack function.

length of the polarization filter. A CSG section is only useful, if the event under consideration is recorded by a large number of stations sampling a sufficient range of hypocentral distances. If stations of a network in a region of high seismicity are distributed rather sparsely, the number of sources may be greater than the number of stations and CRG sections can be advantageous. The alignment and stacking of the S-wave arrival as shown in 2.3b requires the knowledge of the S-wave velocity or the average P-to-S velocity ratio in the studied area. This velocity can be estimated by a stacking velocity analysis similar to the one used in reflection seismics (e.g. Ylmaz, 1987) or vespagram computation in array seismology (e.g. Rost and Thomas, 2002). First, the traces of a seismic section are aligned at the picked first P-wave arrival. Second, for each trace move-out time shifts are computed for an assumed P-to-S velocity ratio, and the shifted traces are stacked using the following formula:

$$S^i = \sum_{i=1}^{N} CF_{sw}^k (t - t^{ik}) \tag{2.7}$$

where N is the number of the traces, and tik is:

$$t^{ik} = t_S - t_P = \frac{\Delta x}{v_P} \left(\frac{v_P}{v_S} - 1 \right) \tag{2.8}$$

where Δ is the hypocentral distance, t_S and t_P are the travel time of S- and P-phase, respectively. Third, this process is repeated for a set of P-to-S velocity ratios. Finally, the velocity ratio that leads to the highest stack amplitude also produces the best phase alignment and thus can be used to estimate the arrivals of the S-waves. Since stacking is done along linear move-out curves, this procedure can be termed linear velocity analysis.

2.3.2   3C analysis

Each three-component seismogram has been rotated from reference system (ZNE) to that of the ray (LQT) using the P-wave incidence angle measured in a 0.3 s time window and the theoretical backazimuth according to the source-receiver geometry. Then the polarization attributes and the characteristic
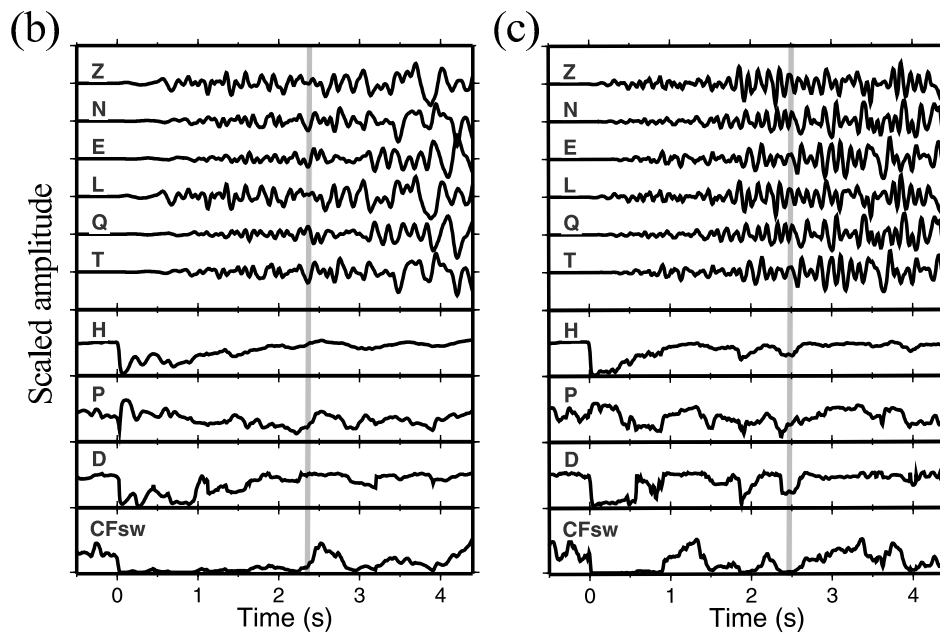
Figure 2.4:   Examples of the three-component processing applied to two different local earthquakes recorded at station SNR3. The gray lines indicate the theoretical arrival times of the S-waves.

function have been computed as described in the Methods section. Figure 2.4 shows the result of the multi-component processing applied to two different local earthquakes recorded at station SNR3. The top six traces are the original and rotated recordings, respectively, and the four traces below are the polarization attributes and the characteristic function CF_{sw}. In Figure 2.4 we can see a good agreement with the theoretical S arrival and the simultaneous increase of H, D, P and CF_{sw}. In particular, the trace does not show significant energy in the time window between the first P-wave arrival (at 0.0 s) and the S-wave arrival (near 2.4 s). However, the event shown in Figure 2.4 is a rather bad example, where the characteristic function shows a strong maximum before the direct S-wave arrival. Probably this maximum corresponds to a converted phase. Looking at just this single recording, the S-wave may not be correctly identified. However, as will be shown in Figure2.5, the seismic sections constructed from the characteristic functions clearly reveals the S-wave, illustrating the relevance of these trace gathers.

2.3.3   S-phase sections

Because the number of earthquakes is much larger than the number of stations, the CF_{sw} traces are collected in common receiver gathers (CRG) to improve the spatial sampling of the entire hypocentral distance range. Then the following seismic processing steps have been applied to all traces of each section. Each trace amplitude is normalized individually to remove the amplitude variations due to the different magnitudes of the events, and due to the amplitude decay with increasing distance. Then the trace envelopes are computed and the mean is removed, which is also a simple but efficient procedure to account for variable polarity. We applied high pass filter to improve visibility of coherent phase on section. Finally, traces with similar hypocentral distance in one CRG are binned and stacked to equalize the distance sampling in that gather. Figure 2.5 shows the resulting CRG sections for the stations VDS3, COL3, CGG3, MNT3, SNR3 and STN3 (see Figure 2.1), together with linear velocity analysis plots. The seismic sections in Figure 2.5 show an excellent
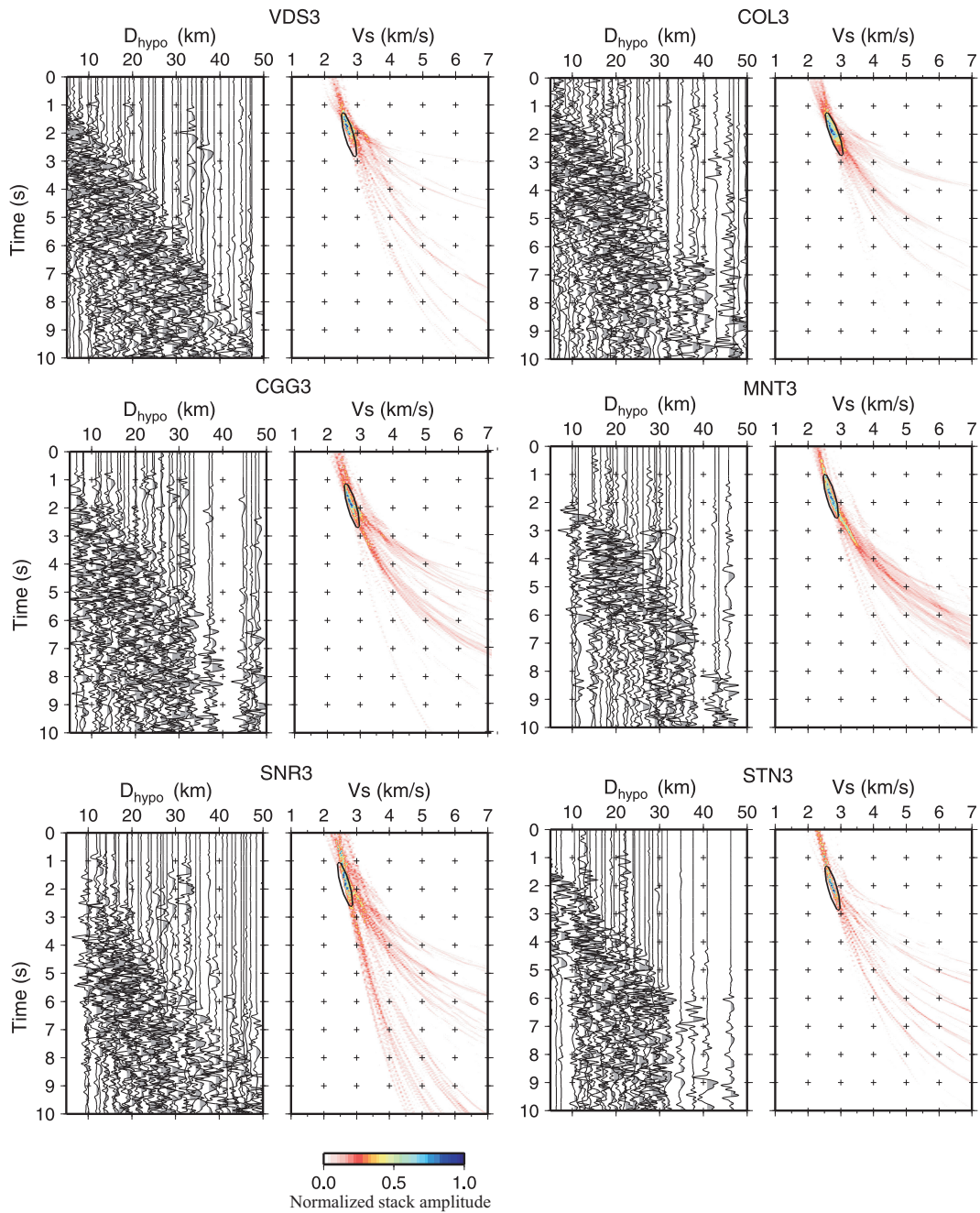
Figure 2.5:   Common receiver gather (CRG) sections and linear velocity analysis panels. For each station, the panel on the left shows the seismic section of the filtered characteristic function , where the traces are aligned at the manual P-wave arrival time picks. The first clear and coherent wave across the whole section is the first S-wave arrival. The panel on the right of each section shows the corresponding linear move-out and stacking velocity analysis in terms of stack amplitude. The stack maxima in blue indicate the best average S-wave velocity for each section. The ellipse is centered on the maximum value.

Figure 2.6:   Signal-to-noise ratio improvement. (a) (b) Comparison of raw transverse-component seismogram sections (left) with the polarization-filtered section (right), which is T multiplied by the characteristic function CF_{sw}. (c) Probability of S/N exceedence for SNR3 and VDS3 stations and for all stations (right).

lateral coherence of the waves as a function of the hypocentral distance. Indeed, a clear first arrival can be seen that coincides with the first arrival of the S-waves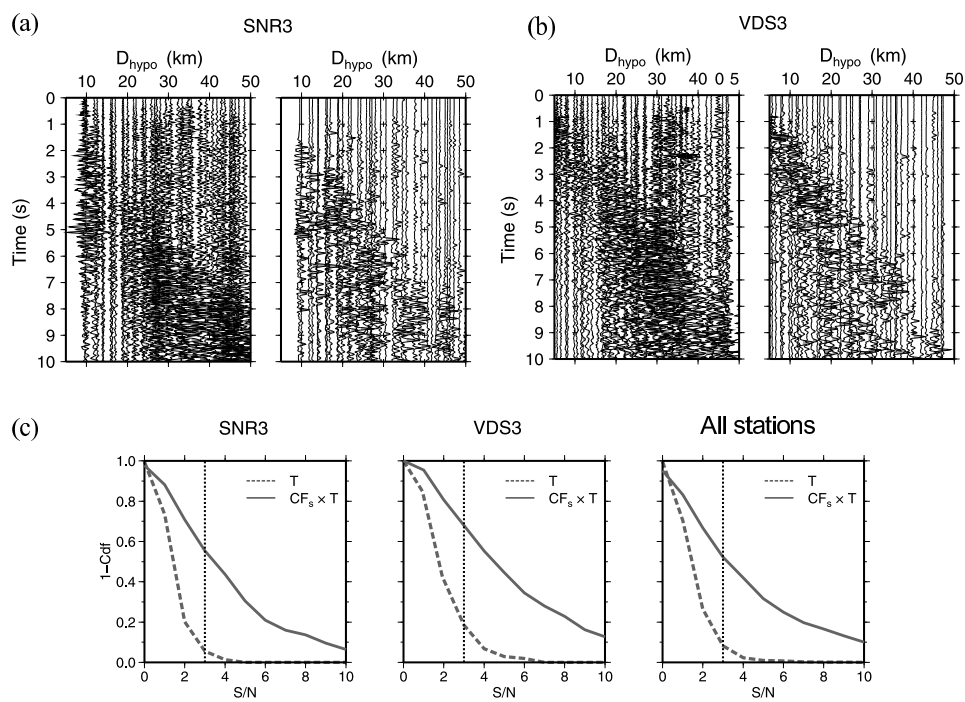. This representation itself already provides a useful arrangement for visual identification of the S-waves. The panels on the right of each seismic section in Figure 2.5 show the results of a linear move-out and stacking velocity analysis for the corresponding sections in terms of the color-coded stack amplitude. Each stack maximum (blue in Fig. 2.5) indicates the optimal average S-wave velocity for the respective section. In Table 2.1 we provide the velocity range with normalized stack amplitude greater than 0.75 for each analyzed station. The average velocity is around 2.7 km/s and the lateral velocity variation is small.

Station	V_s range km/s	$P(S/N \geq 3)_T$ [%]	$P(S/N \geq 3)_{CFxT}$ [%]
AVG3	$2.59 \div 2.85$	0	35.7
BEL3	$2.49 \div 2.11$	2.1	57.4
CGG3	$2.55 \div 3.00$	7.00	28.6
COL3	$2.59 \div 2.83$	8.6	54.0
CSG3	$2.60 \div 2.86$	4.5	64.7
MNT3	$2.53 \div 3.20$	1.2	58.9
NSC3	$2.55 \div 2.80$	3.4	44.7
PGN3	$2.49 \div 3.15$	3.4	27.4
SNR3	$2.54 \div 3.06$	5.5	55.4
SRN3	$2.54 \div 3.06$	9.5	49.3
STN3	$2.54 \div 2.90$	7.9	73.2
TEO3	$2.44 \div 2.86$	15.4	56.5
VDS3	$2.59 \div 2.96$	18.5	68.0

Table 2.1: S velocity and probability of S/N exceedence for raw and filtered T-component seismograms.

Figure 2.6 illustrates the overall improvement of the signal-to-noise ratio (S/N) on seismic sections due to the application of the proposed polarization
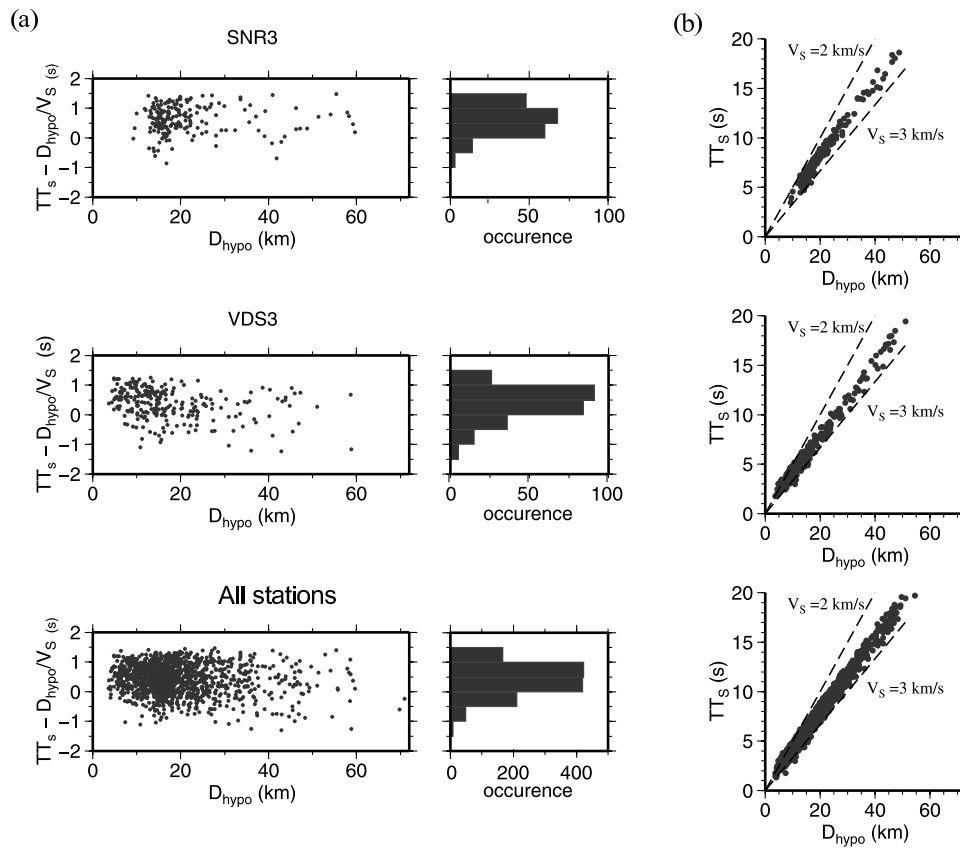
Figure 2.7: Travel time residuals. (a) Residuals as a function of hypocentral distance for two stations and for all stations. (b) S-wave travel time curves.

filtering procedure. For each station, the left-section shows the transverse-component seismograms and the right-section represents transeverse-component multiplied by the characteristic function CF_{sw} . To quantify the S/N improvement we represent in Fig. 2.6c the probability to have a S/N larger then a given threshold value. The S/N is computed by using the signal RMS amplitude value in a 2 s time window after the S-wave arrival time the noise RMS amplitude in a 1 s window before the S-arrival time (i.e the P-wave coda). Then we compute the normalized cumulative histogram Cdf of S/N and convert this to a probability of exceedence by plotting 1 Cdf. Figure 2.6c shows the probabilities for the two stations and for all stations (right). The dashed line is the probability for the transverse-component section, and the solid line the probability for the corresponding polarization-filtered section. For station SNR3 the probability to observe a S/N larger than 3 (dotted line) increases from 5.5% to 55.4% and at VDS3 from 18.5% to 68%. Table 1 summarizes the probability of exceedence for a S/N value egual to 3, for all stations before and after polarization filtering, and respectively. The improved S/N makes it easier to identify the S phase on the polarization-filtered sections than on the original seismograms. To verify that the identified phase is in fact an S wave, we picked the first arrivals on the sections and calculate theoretical S arrival times based on the measured velocities. Figure 5a shows the residuals as a function of hypocentral distance for SNR3, VDS3 and for all stations, and the travel times vs distance are shown in Figure 12.7. Qualitatively, the distributions of the residuals and the travel times indicate the consistency of the identified S-wave arrivals.

2.4 Refined re-picking based on cross-correlation method

In order to obtain highly accurate readings the automatic refined re-picking technique proposed by Rowe et al (2002) has been used. The technique uses an algorithm for estimating the relative time delay, which is based on the

similarity of the waveforms.

2.4.1 Technique

The used method may be outlined as follows:

- Data organization;

- Clustering catalogue based on waveform similarity;

- Adaptive window-length cross-correlation within clusters;

- Solving for consistent pick lags within clusters;

- Monte Carlo error estimations.

Prior to processing, waveforms must have a preliminary picks, and are analyzed from many events on a station-by-station basis. Once the data are have been properly formatted, a preliminary cross-correlation is performed. The retrieved cross-correlation values for each pair of waveforms is used to divide the catalogue into clusters of highly similar events. This subdivision, or clustering, is followed by relative lag estimation among member traces within a cluster using an adaptive time window length. After all possible waveforms comparison has been made, the resulting, ovedetermined system of individual event lags may be solved to obtained consistent pick adjustement and associated uncertainties. This is obtained using an iterative conjugate gradinet approach, while the 1-sigma error bars are calculated via a Monte Carlo pertubation of the data vector.

2.4.2 Application to P and S dataset

The waveforms of all analyzed seismic events have been organized by station-common gathers. The preliminary P-pick correspond to the manual pick on vertical component; the preliminary S-pick was obtained manually revising all the horizontal components using the characteristic function described in the

section 2.2. For each pair of traces recorded at the same station, the similarity was evaluated by using cross-correlation function in a window around the reference pick. The choice of the appropriate time window for the cross-correlation is assessed through preliminary tests. In particular, the distribution of cross-correlation coefficients for each pair of waveforms is analyzed to varying the length of the window. The optimal time window correspond to the window which allows to have the largest number of couples with a cross-correlation value greater than 0.5. This criterion leds the choice of 0.5 s and 1.0 s time window for the P- and S-phase, respectively. Based on the degree of similarity as assessed using cross-correlation coefficient, the catalog is divided into clusters. The traces orphan are discarded from the analysis and all the waveforms belonging to a cluster are again cross-correlated. Even in this case an automatic procedure allows the choice of the appropriate duration of the cross-correlation time window. At this step the result is an amount of time that must be added or subtracted to the all waveforms belonging to the same clusters. These delay time are inverted using an iterative technique to the conjugate gradient (Aster and Rowe, 2002, Rowe et al., 2002). The error is estimated by Monte Carlo method. The end result is a correction to be made to the initial reference time of the pick.

In Figure 2.8 the result obtained for six different clusters is shown. In particular, panel a) shows the results for the picking P while panel b) those for picking S. An improvement in the waveforms reallineamente and their stack traces (blue curve and red curve) is observed when moving from manual to refined pick.

2.5   Modified Wadati diagram

The final catalog consists of 5078 P and 2071 S readings corresponding to 479 earthquakes. An evaluation of picking consistency has been performed analyzing the *modified Wadati diagram* (Chatelain, 1978), which also provides an estimate of an average VP/VS ratio. The differences between $T_{P_i} - T_{P_j}$ and
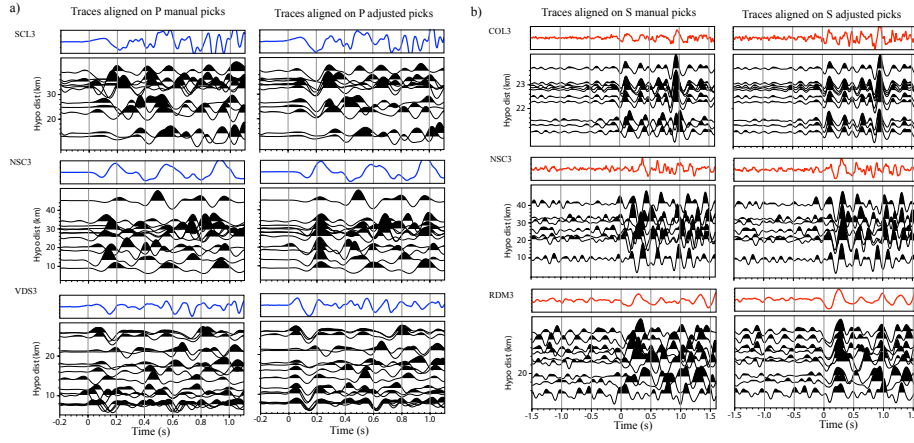
Figure 2.8:   Waveforms cluster at stations COL3, SCL3, NSC3, and RDM3 VDS3 (see Figure 2.1): Panel a) shows the alignment of vertical component with respect to the manual pick P (left panel) and pick P refined (right panel), while panel b) we show sthe alignment of the horizontal components compared to manually pick S (left panel) and the refined re-pick (right panel).

$T_{S_i} - T_{S_j}$ arrival time, for each event, for each couple of station are evaluated and represented on a diagram in which each point does not depend on the origin time. Assuming an homogeneous half space, the differences between the P and S arrival time are related through the following equation

$$T_{S_i} - T_{S_j} = \frac{V_P}{V_S} T_{P_i} - T_{P_j} \tag{2.9}$$

and using a least square fitting line it's possible to estimate a value for the V_P/V_S ratio. The inferred V_P/V_S ratio value is equal to 1.88 (Figure 2.9).

2.6   Earthquake relocations

Using the 1D reference model for the area (Matrullo, 2012) and the estimated V_P/V_S ratio we performed a relocation of the events using before only the refined P reading (Figure 2.10a) and than using P and S refined readings (Figure 2.10b). The mean value of the horizontal and vertical location errors, reported in Figure 2.11, improve utilizing P and S reading.
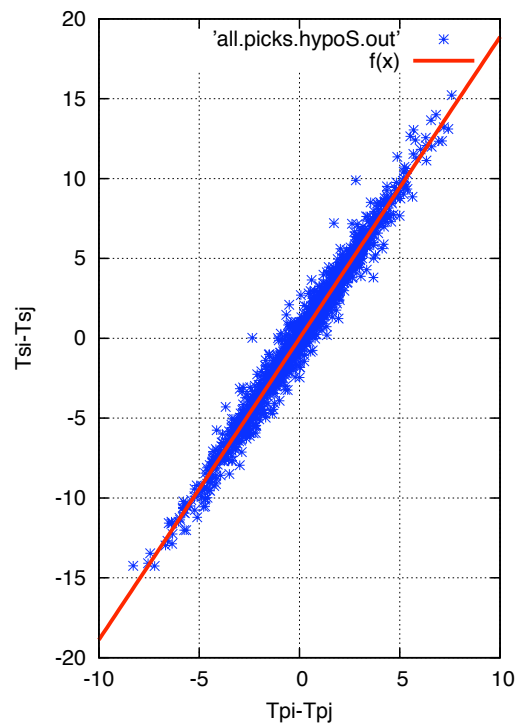
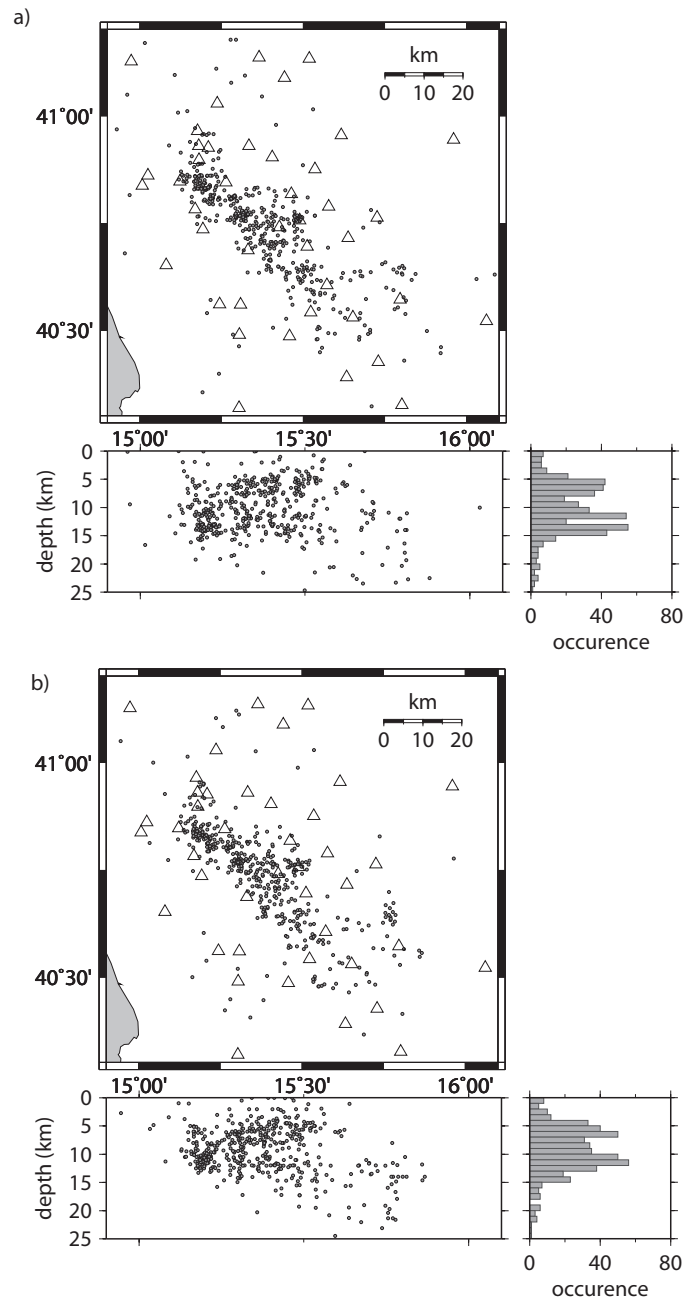Figure 2.9:   Simil Wadati diagram. The best fit line (in red) correspond to a V_P/V_S ratio of 1.88.

Figure 2.10: Epicentral distribution and vertical section of the relocated events using a) only P refined re-picking and b) using P and S refined re-picking.
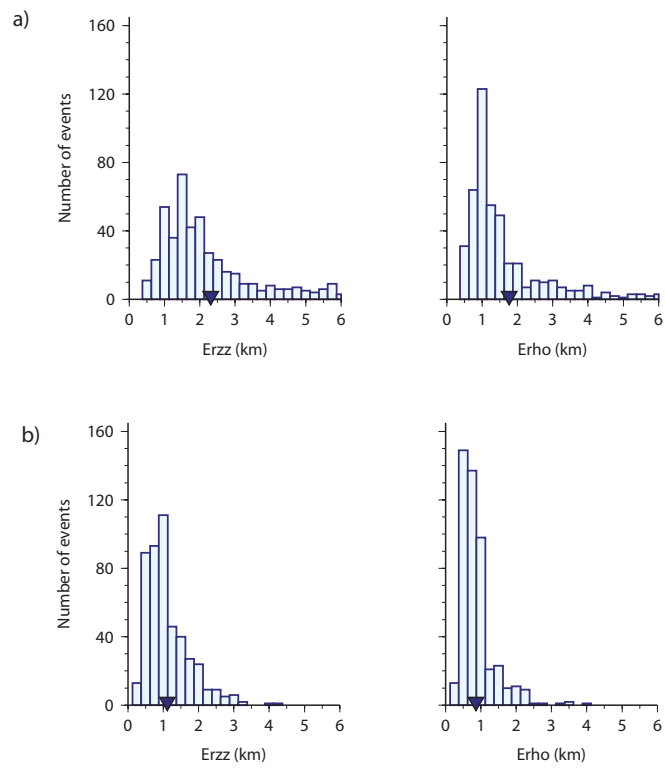
a)

b)

Figure 2.11:   Horizontal and vertical error relative to the earthquake location of
the events repicked with refined technique, using P a) and P and S refined re-picking.

Chapter 3

Tomographic inversion procedure and approach

3.1 Introduction

The use of local earthquakes for the tomographic inversion of delay times
in a region affected by strong earthquakes, can provide a three-dimensional
image of seismic velocity models. These models allow to study the relation-
ship between the behavior of a fault and the physical-mechanical properties
of the host environment (Michael and Eberhart-Phillips, 1991). In particular,
Thurber et al., 1995 have emphasized the relationship between the V_p/V_s pa-
rameter and changes in physical properties of the rocks in seismogenic areas.
The location of earthquakes provides a primary information about the geome-
try of the structures on which they are generated allowing to study the possible
correlation of these structure with the destructive earthquakes occurred in the
past. The accuracy of the location techniques with the absolute time is criti-
cally controlled by several factors, among which the geometry of the network,
the number of available phases, the accuracy of arrival the times and the
knowledge of the crustal structure (Pavlis, 1986). For example, the use of a
one-dimensional reference model can affect the accuracy of the location. This
is because the three-dimensional heterogeneities of the propagation medium

introduce systematic errors in the estimation of traveltimes. In order to partially reduce the effect of using a 1D velocity model, the double differences location techniques can be used. The idea behind these technique is to minimize the effect of poor knowledge of the structure based on the assumption that two events, very close in space, recorded at the same station travel along the same path, thus the contribution of the seismic velocity can be eliminate from the equation of double differences Waldhauser and Ellsworth, 2000. However Michelini and Lomax, 2004 emphasize that the use of these methods is not possible without an accurate knowledge of the velocity model. Only the joint inversion of hypocenter and velocity parameters allow to overcome the simplistic assumptions of the location methods mentioned above. The methods used today for the joint tomographic inversion have made substantial progress with respect to the basic concept expressed by Aki and Lee, 1990. These methods include techniques for 3D ray tracing calculation of the traveltime field by the integration of slowness along the ray (Latorre et al., 2004), the use of S waves, for which the times can be inverted either alone or simultaneously with the P waves to obtain the ratio V_p/V_s, and direct inversion of the ratio Q_p/Q_s. A very important trend is that of double differences, through the use of them Zhang and Thurber, 2005 show that a significant improvement in tomographic image can be achieved when the technique is combined with the relative arrival times. Monteiller et al., 2005 accompanying the double differences with the Tarantola-Valette (Tarantola and Valette, 1987) approach pointed out that a necessary conditions for the use of double difference tomography is the availability of an initial three-dimensional model.

In this chapter the general principles of tomography of the delay times, in relation to the techniques implemented in the inversion code used in this work are described.

3.2 Problem formulation

The body wave travel time T from an earthquake i to a seismic station j is expressed using ray theory as a path integral Thurber, 1993

$$T_{ij} = \int_{source}^{receiver} u\,ds \tag{3.1}$$

where u is the slowness field (reciprocal velocity) and ds is the elementary path length. The actual observations are the arrival times t_{ij}, where

$$t_{ij} = \tau_i + T_{ij} \tag{3.2}$$

and τ_i is the earthquake origin time. In terms of inverse problem (Menke, 1989) the observed arrival times are the data, the source coordinates, the origin times, the ray-paths, and slowness field are the unknowns (model parameters). Given a set of arrival times t_{ij}^{obs} measured at a network of stations, the calculated arrival times t_{ij}^{cal} are determined from equations 3.1 and 3.2 using trial hypocenters and origin times and an initial seismic velocity model. The mistfit between observed and predicted (calculated) arrival times are then the residuals r_{ij}

$$r_{ij} = t_{ij}^{obs} - t_{ij}^{cal} \tag{3.3}$$

The residulas can be related to the desired perturbation to both the hypocenter and velocity model by using a linear approximation

$$r_{ij} = \sum_{k=1}^{3} \frac{\partial T_{ij}}{\partial x_k}\Delta x_k + \Delta\tau_i + \int_{source}^{reciever} \delta u\,ds \tag{3.4}$$

All the linearized local earthquake tomography methods are based on equation 3.4 and then diversify to some extent, on the basis of the different treatment of some or all of the following aspects of the problem:

- the scheme adopted for representing of the velocity model;

- the technique for travel time and ray-path calculations;

- the treatment of the hypocenter-velocity structure coupling;

- the inversion procedure.

3.2.1   Representation of the velocity structure

The Earth's crust has heterogeneous structure on a vast range of spatial scales, including complications such as discontinuities, faults, layering, intrusions, inclusions, zones of elevated temperature or partial melt, and random geological heterogeneities. The spatial scale of heterogeneity that can be imaged through the local earthquake tomography depends on the density of ray sampling, with a lower bound proportional to the minimum wavelength of recorded seismic wave energy. Model parametrization of the velocity model should be able to delineate, as much as possible, shape and position of heterogeneities. A nodal representation, in which the velocity filed is reconstructed by a three-dimesional grid, does not assume a specific geometry of heterogeneities. In the nodal representation the velocity perturbation filed (or the slowness filed) $\delta u(x, y, z)$ can be described with a meshed cube regularly spaced in the three directions, is the specified at each node a value $u_{m,l,n}$ and the following functions are used:

$$\delta u(x, y, z) = \sum_{cube} \delta u_{m,l,n} h_{m,l,n} \tag{3.5}$$

where

$$h_{mln} = \begin{cases} 1 & \text{at node} \\ 0 & \text{otherwise} \end{cases} \tag{3.6}$$

The equation 3.4 thus becomes

$$r_{ij} = \sum_{k=1}^{3} \frac{\partial T_{ij}}{\partial x_k} \Delta x_k + \Delta \tau_i + \sum_{cube} \frac{\partial T_{i,j}}{\partial u_{m.l,n}} \Delta u_{m,l,n} \tag{3.7}$$

Because no single scheme can faithfully represent all the aspects of the crustal heterogeneities, a good inversion strategy is a *multiscale* approach: a series of inversions is run by progressively refining the velocity grid, the starting model for each inversion being the final model for the previous one. This procedure, which was first introduced for velocity estimation by Lutter et al., 1990, allow us to determine the large-scale components of the velocity model and then to progressively estimate the smaller-scale components.

3.2.2   Ray-path and travel time calculation

One of the practical problems that must be solved in seismic tomography is the determination of the propagation path of the seismic waves between each source-receiver pair, and the wave traveltime along that path. The travel time is needed in order to calculate the arrival time residual, while the path is needed for computing the hypocenter and velocity partial derivatives.

There are many technique for determine ray paths and traveltimes. The estimate of fisrt-arrival traveltimes by Podvin and Lecomte, 1991 algorithm requires a finer grid of cubic cells because the technique assumes constant slowness in each cell. These slowness values are deduced by trilinear interpolation of the inversion grid. For each station, the solution of the eikonal equation provides a first estimation of traveltimes at each node of the finer grid. By following the gradient of the estimated traveltimes, it is thus possible to trace the ray back from the source to the receiver. After this a *posteriori* ray tracing, the finer grid is no longer used.

Once the rays are computed for each event-receiver pair, more precise traveltimes are recalculated by performing a numerical integration of the slowness filed along the rays. Simultaneously, for each node of the inversion grid, traveltime partial derivatives are computed for P and S slowness fileds, hypocentre location and origin time (see 3.7). Latorre et al., 2004 have demonstrated that traveltimes obtained with this procedure are less sensitive to the grid spacing used for the wave front traveltime computation.

3.2.3   Hypocenter-velocity structure coupling

One of the nagging questions in tomography is the proper treatment of the mathematical coupling between hypocenter parameters and the velocity model that is apparent in equation 3.7. Traditionally, the term local earthquake tomography has usually implied the determination of three-dimensional velocity structure keeping hypocenter parameters fixed at their inital values, while simultaneous inversion is usually construed to mean explicit treatment of the

hypocenter-velocity structure coupling.

If N earthquakes and M stations are considered, the equation 3.7 must be written for each couple station-earthquake. As a consequence we have an equations system is setup in which the residual times (data) are linked to the hypocentral parameters and the velocities at each grid node (parameters) through the partial derivatives of the residual respect to the parameters. This can be illustrated by following formula:

$$
\begin{pmatrix} r_1 \\ r_2 \\ r_3 \\ \vdots \\ \vdots \\ \vdots \\ \vdots \\ r_n \end{pmatrix} = \begin{pmatrix} \frac{\partial T_{11}}{\partial u_1} & \frac{\partial T_{12}}{\partial u_2} & \frac{\partial T_{13}}{\partial u_{13}} & \cdots & \frac{\partial T_{11}}{\partial x^1} & \cdots \\ \cdots & \cdots & \cdots & \cdots & \cdots & \cdots \\ \cdots & \cdots & \cdots & \cdots & \cdots & \cdots \\ \cdots & \cdots & \cdots & \cdots & \cdots & \cdots \\ \cdots & \cdots & \cdots & \cdots & \cdots & \cdots \\ \cdots & \cdots & \cdots & \cdots & \cdots & \cdots \\ \cdots & \cdots & \cdots & \cdots & \cdots & \cdots \\ \cdots & \cdots & \cdots & \cdots & \cdots & \cdots \\ \cdots & \cdots & \cdots & \cdots & \cdots & \cdots \\ \frac{\partial T_{n1}}{\partial u_1} & \frac{\partial T_{n2}}{\partial u_2} & \frac{\partial T_{n3}}{\partial u_{13}} & \cdots & \frac{\partial T_{n1}}{\partial x^1} & \cdots \end{pmatrix} \begin{pmatrix} \delta u_1 \\ \delta u_2 \\ \delta u_3 \\ \vdots \\ \delta u_m \\ \delta x^1 \\ \delta y^1 \\ \delta z^1 \\ \delta \tau^1 \\ \vdots \end{pmatrix} \tag{3.8}
$$

or in a compact notation

$$
\mathbf{r} = \mathcal{A}\delta\mathbf{u} \tag{3.9}
$$

The direct treatment of the hypocenter-velocity structure coupling requires that the parameters should be inverted all together without using any parameters separation technique.

Scaling operation

Before solving the linearized system, the units used for different parameter quantities must betaken into account. The P-wave velocity has the same units as the S-wave velocity while hypocenter parameters (source coordinates and origin time) have quite different units, changing this units will modify the shape of the misfit function. The definition of the weighting which makes one class of

parameters more or less sensitive to the data is performed through synthetic examples assuming the real configuration of station and seismic sources, in fact the different weights depend on the geometry of each experiment.

3.2.4   Inversion method

One of the methods used to solve the equation 3.9 consist in finding a solution in the sense of least squares, which search the vector x which minimizes the function

$$min\|Ax - b\|_{L2} \tag{3.10}$$

Since the problem is underdetermined the solution may not be unique; it is therefore necessary to introduce a regularization which is an additional condition that allows the convergence towards a single solution. A classical approach to solve the underdetermined problems is to search for a solution in sense of the damped least-squares (Menke, 1989). The system to be solved becomes

$$\begin{pmatrix} A \\ eI \end{pmatrix} x = \begin{pmatrix} d \\ 0 \end{pmatrix} \tag{3.11}$$

where I is the identity matrix and e is the parameter that controls the degree of damping. This parameter defines the damping of the perturbation amplitudes compared to the reference model, otherwise known as the distance between the initial parameters and the final parameters of the model. This value controls the relationship (*trade-off*) between the standard deviation of the data (*misfit*) and the variance of the model obtained.

The equation 3.10 can be written as

$$min\|Ax - b\|_{L2} + \|\epsilon I x\|_{L2} \tag{3.12}$$

And the final solution is

$$\vec{x} = \left(A^T A + \epsilon^2 I\right)^{-1} A^T b \tag{3.13}$$

Damping

The damping parameter defines the perturbation amplitudes respect to the reference model, ie the distance between the initial parameters of the model and final parameters. If a too high value of damping parameter increase the mistfit, a too small value makes it better, but increases the variance of the model and leads to a solution physically impossible. Physically, the damping parameter affects the solution of the inversion and uses choice requires a preliminary study. The damping value can be selected based on an empirical approach. For each data set, several one-step inversions were run with different damping values. Then the reduction in data variance is compared to the variance of the solution. The selected value was the one which greatly reduced the data variance with a moderate increase in the solution variance.

3.3   Description of the tomographic inversion procedure

We used an iterative, linearized, damped, tomographic approach (LeMeur et al., 1997, Latorre et al., 2004, Vanorio et al., 2005, Battaglia et al., 2008) in which the arrival times of P and S are simultaneously inverted for the earthquakes location and velocities distribution (Thurber, 1992). The parameterization of the model is performed by nodal representation: the velocity value is assigned to the vertices of a grid with regular spacing. The code for the tomographic inversion used is TOMO_ TV, and was developed during the thesis by the Professor J. Virieux of Joseph Fourier University in Grenoble, and adapted by me, implemented it and verified through a series of numerical tests on synthetic and real data. Each iteration consist of the following operations:

- trilinear interpolation of the velocity model in a finer grid;

- calculation of the theoretical arrival times with the technique of finite difference Podvin and Lecomte, 1991, in order to obtain a first estimate

for each station of the traveltime at each node of the grid finer of 0.5 x 0.5 x 0.5 km^3;

- ray tracing technique of back ray-tracing for each source-receiver pair along the gradient of the traveltime estimates;

- accurate calculation of the traveltime field by integration of slowness along the ray path Latorre et al. (2004);

- calculation of the partial derivatives of the traveltime field simultaneously for P and S slowness, hypocentral coordinate and origin time of earthquakes;

- preconditioning and smoothing of the matrix of derivatives. The first is the normalization and scaling of the matrix of derivatives in order to control the quality of estimated parameters. This operation is controlled by a set of four hyper-parameters (Cp, Cs, Cp0, CT0), one for each class of parameters to be estimated. The smoothing is achieved by requiring that the Laplacian of the slowness field is zero (Benz et al., 1996);

- inversion of linear system of equations, scaled and weighed, with the algorithm LSQR (Paige and Saunders, 1982).

The regularization of the inversion is achieved by the damping factor.

3.4 Inversion parameters tuning

As we have seen in order to obtain the solution of an under-determined inverse problem in the least squares sense requires the definition of a damping factor. In addition, the joint inversion of different classes of parameters requires the conditioning of the matrix of partial derivatives among the weighting factors called *hyper-parameters*. The calibration of these factors is a necessary step to do before the real data inversion. This operation is important for the tomography process as they may significantly influence the final results.

To determine the optimal combination of hyper-parameters should be carried out synthetic tests, however, the choice of the damping factor must be made through the inversion of real data in order to compare the variance of the data compared to the variance of the model.

3.4.1   Hyper-parameters

To determine the optimal combination of hyper-parameters we performed a sensitivity test, ie synthetic tests using the real earthquakes-station configuration and the same parameters chosen for the tomographic inversions. Synthetic P and S velocity model are designed by adding two velocity anomalies, one positive (+1000m/s) and one negative (-1000m/s) with elliptical shape, in the central part of the models within an homogeneous velocity model (Figure 3.1). Theoretical traveltimes are computed in these models and are used as
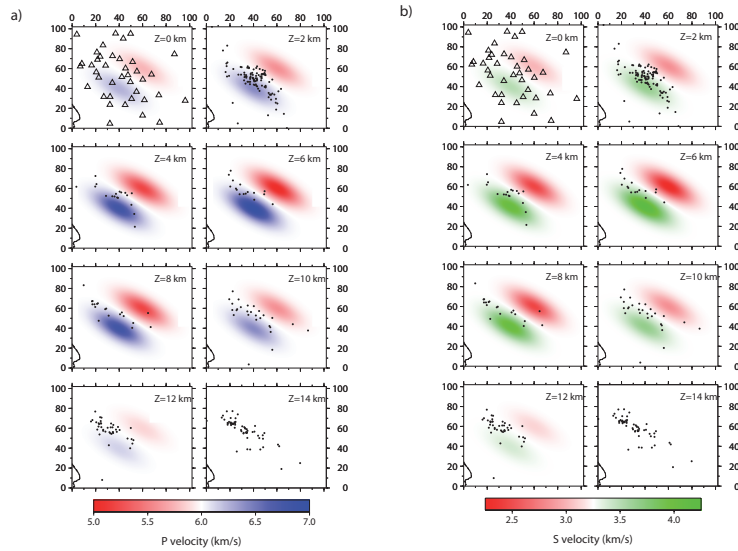

Figure 3.1:   Synthetic velocity models P (a) and S (b).

observed times. Homogeneous velocity models are considered as initial mod-

els and earthquake are relocated to obtain an initial hypocenter location. We performed several inversions for several combinations of hyper-parameters and observing the evolution of the difference between the final model obtained and the true model in function of the number of iterations, we chose the combination of parameters for which the trend of this curve is convergent for all four classes simultaneously. In Figure 3.2 the curve represented the variance in function of the iteration number are reported for five different combination of hyper-parameters, Cp, Cs, Cp0 and CT0. The selected values, represented by the blue line, are Cp= 1, Cs= 1, Cp0= 6 and CT0= 6.
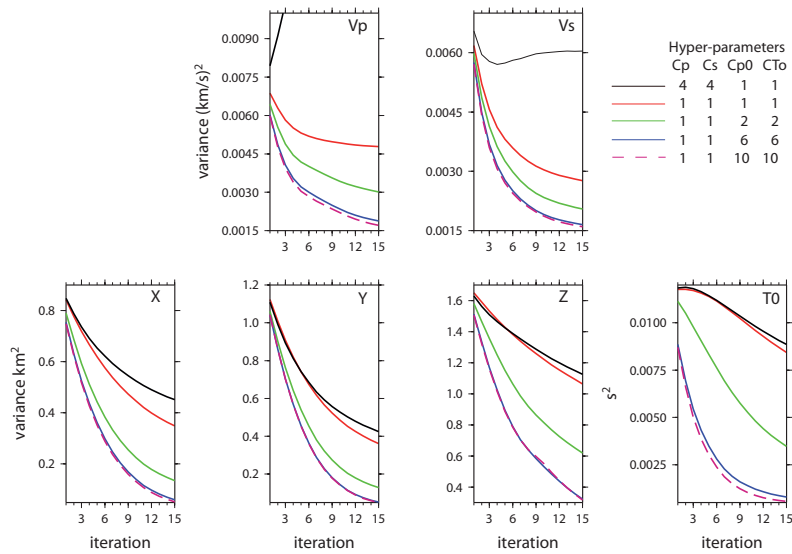

Figure 3.2: Variance in function of iteration number for each parameter inverted to varying combinations of different hyper-parameters.

3.4.2 Damping factor

For the calibration of the damping factor we followed an empirical approach (Eberhart-Phillips, 1986). Using real datasets P and S arrival times, we per-

formed several inversions for different values of damping. We then compared
the variance of the data with the variance of the model, creating for each class
of parameters to estimate the trade-off curves (Figure 3.3). The value chosen
is the value of damping for which a small variance in the data corresponds to a
small variance of the model, for all four classes of parameters simultaneously.
The selected value correspond to 0.7.

3.5   Inversion strategy

In order to obtain a velocity structure the inversion strategy follows a multi-
scale approach.
The linearized inversions requires the choice of a starting velocity model close
to the reality. The 1D Vp velocity model optimized for the area is used.

3.5.1   1D initial velocity model

The used 1D Vp velocity model proposed by DeMatteis et al., 2011 was ob-
tained following the approach of Kissling et al., 1994, in which a P-wave Min-
imum 1D velocity model is computed by a joint inversion of layered velocity
model, station corrections and hypocenter locations. The used data correspond
to a sub-dataset of the whole dataset of P manual readings analyzed in this
work (Matrullo, Amoroso, Matteis, Satriano, and Zollo, Matrullo et al.). The
retreived Minimum 1D model (Figure 3.4) presents a P-wave velocity shallow
layer (until 2 km depth) of 3.25 km/s. This is consistent as average P-wave
velocity value due to the known strong lateral velocity variations due to differ-
ent lithologies varying from Carbonate Platoform domain (P-wave velocity of
5.3 ÷6.0 km/s) to thrust sheet- top clastic sequence (P-wave velocity of 2.01÷
2.4 km/s). A layer of 4 km (from 2 to 6 km in depth) is caracterized by a
velocity of 4.72 km/s compatible with the seismic velocity of the Lagonegro
Basins units (Improta et al., 2003). The layer velocity layer from 6 km to
12 km depth is representative of Apulian Platform domain (Improta et al.,
2003, Boncio et al., 2007). Then the velocity smoothly increases with depth,
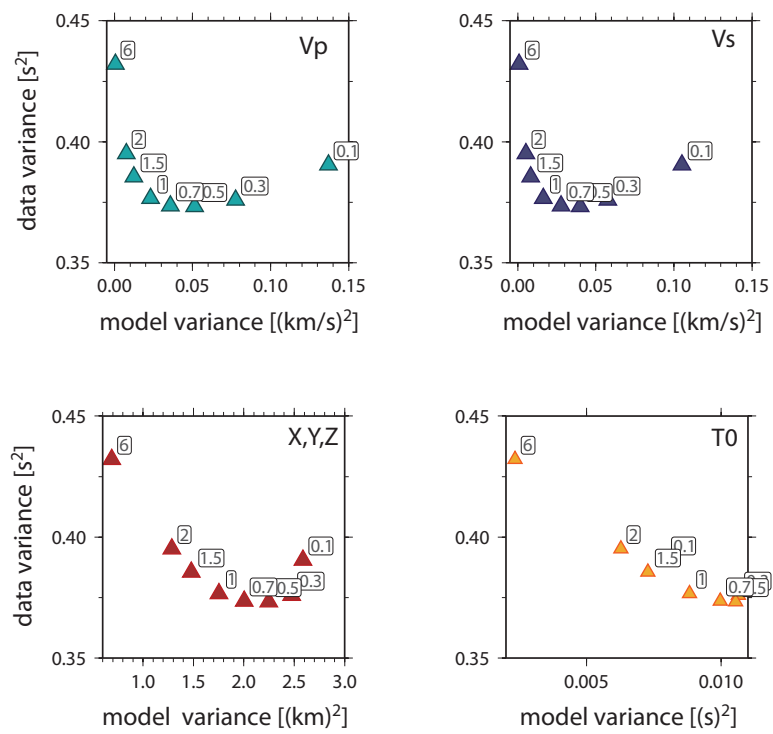
Figure 3.3:   Trade-off curve for selecting optimal value for real data set. The data variance and solution variance are computed after one iteration for indicated damping values.

in agreement with the typically Basement velocities, until 35 km where the Moho is espected. The distribution of station correction shows a strong lateral variation in direction othogonal to the Apenninic chain (Figure A.1), a physical interpretation is provided in the Appendix A.
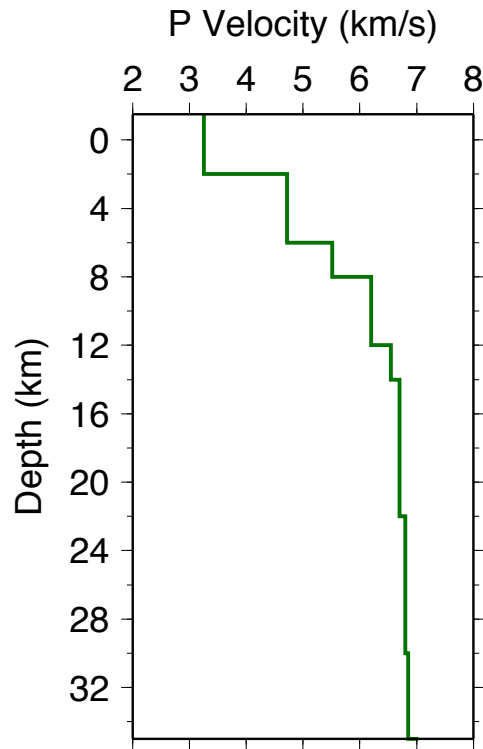

Figure 3.4:   1D reference Vp velocity model optimized for the area under study DeMatteis et al., 2011

Vp/Vs estimation

In order to obtain a starting Vs velocity model the adopted strategy consist of the following operation:

- determination of a 3D P velocity model by the inversion of real dataset;

- conversion of the 3D P velocity model in 3D S velocity models by using different Vp/Vs ratio ranging from 1.65 to 2.00;

- calculation of traveltime residuals for the S velocity model derived from the P model;

- analysis of the RMS respect to the Vp/Vs values.

The parabolic shape of the curve of RMS *vs* Vp/Vs, reported in figure 3.5 exhibit the presence of a minimum value for RMS which corresponds to the optimal value. The latter correspond to Vp/Vs equal 1.82. This value is consistent with the result obtained in other studies in the same region (Maggi et al., 2009; DeMatteis et al., 2012).
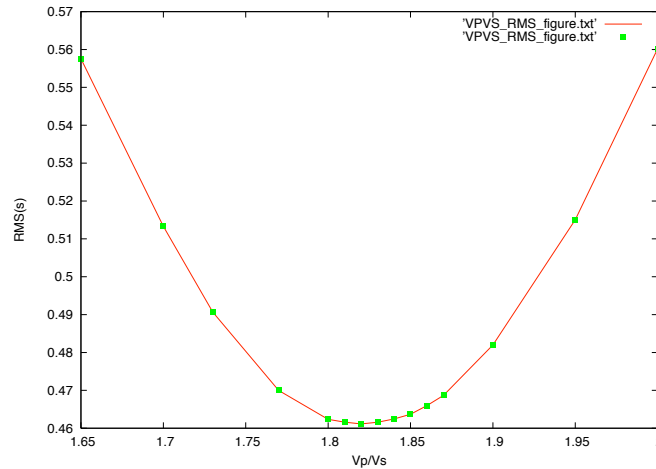

Figure 3.5: RMS of S travel time residual *vs* Vp/Vs.

3.5.2 Multiscale approach

The stations/events distibution allows us to investigate a volume of 100x 100x30 km^3. The velocity model parametrization is performed by a nodal

representation, described by a tridimensional grid (Dx, Dy, Dz). The inversion strategy is based on a multiscale approach (Bunks et al., 1995), a series of inversion progressively decreasing the grid spacing are performed. The starting model for each inversion being in the final model of the previous one. This procedure allow us first determine the large-scale components of the velocity model and then to estimate progressively the smaller-scale component (Lutter and Nowack, 1990; Zollo et al., 2002). The procedure was validated by synthetic tests, we have, in fact, verified that using multiscale approach can properly reconstruct small and large anomalies. In particular we before realize a synthetic P and S velocity model by adding two velocity anomalies, one positive ($\pm 1000 m/s$) and one negative ($\pm -1000 m/s$) with elliptical shape, in the central part of the models within an homogeneous velocity model (Figures 3.6a 3.7a). Theoretical traveltimes are computed in these models and are used as observed times. Homogeneous velocity models are considered as initial models and earthquake are relocated to obtain an initial hypocenter location. We perform several inversions progressively decreasing the grid spacing. In particular the used parametrization are 12x12x4 km^3, and 6x6x2 km^3 3x3x1 km^3 and the recovered pattern are displayed in Figures 3.6b 3.7b. Following the same procedure we tried to reconstructed a velocity model designed by checkerboard anomalies. They are generated using a sinusoidal function having a wavelength corresponding to 3x3x1 km^3 (Figure 3.8a). The synthetic pattern is well recovered at the end of multiscale inversion in the central part of the model compatibly with ray coverage.

3.5.3   Assessment of solution quality

Checkerboard tests are commonly used to assess model resolution in tomographic studies. A checkerboard model consists of an alternating anomaly pattern of positive and negative regions superimposed on the final, initial or on an average one-dimensional velocity model. Relatively small velocity perturbations can be used, so that ray paths through the model are minimally perturbed compared to the background model. But the velocity perturba-
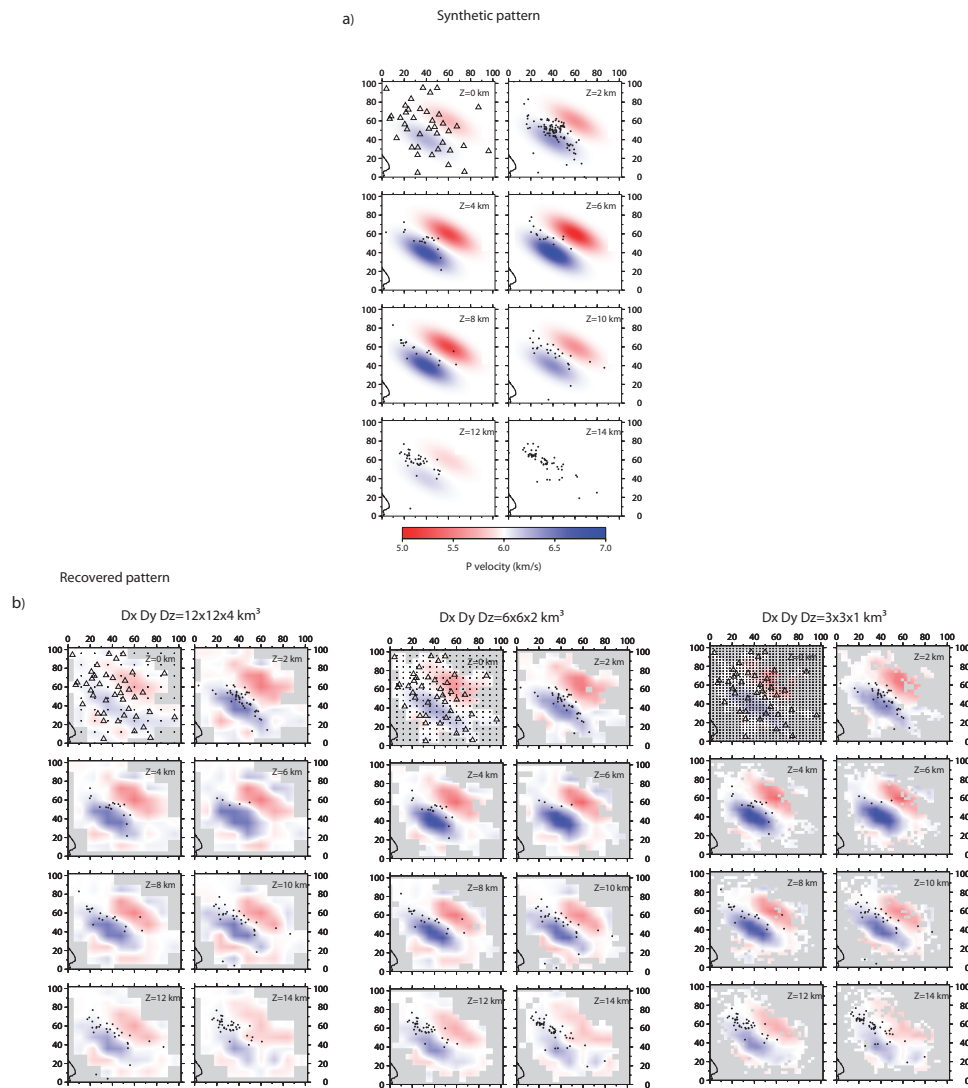
Figure 3.6: Multiscale approach: synthetic test for P velocity model. a) Synthetic pattern. b) Recovered pattern.
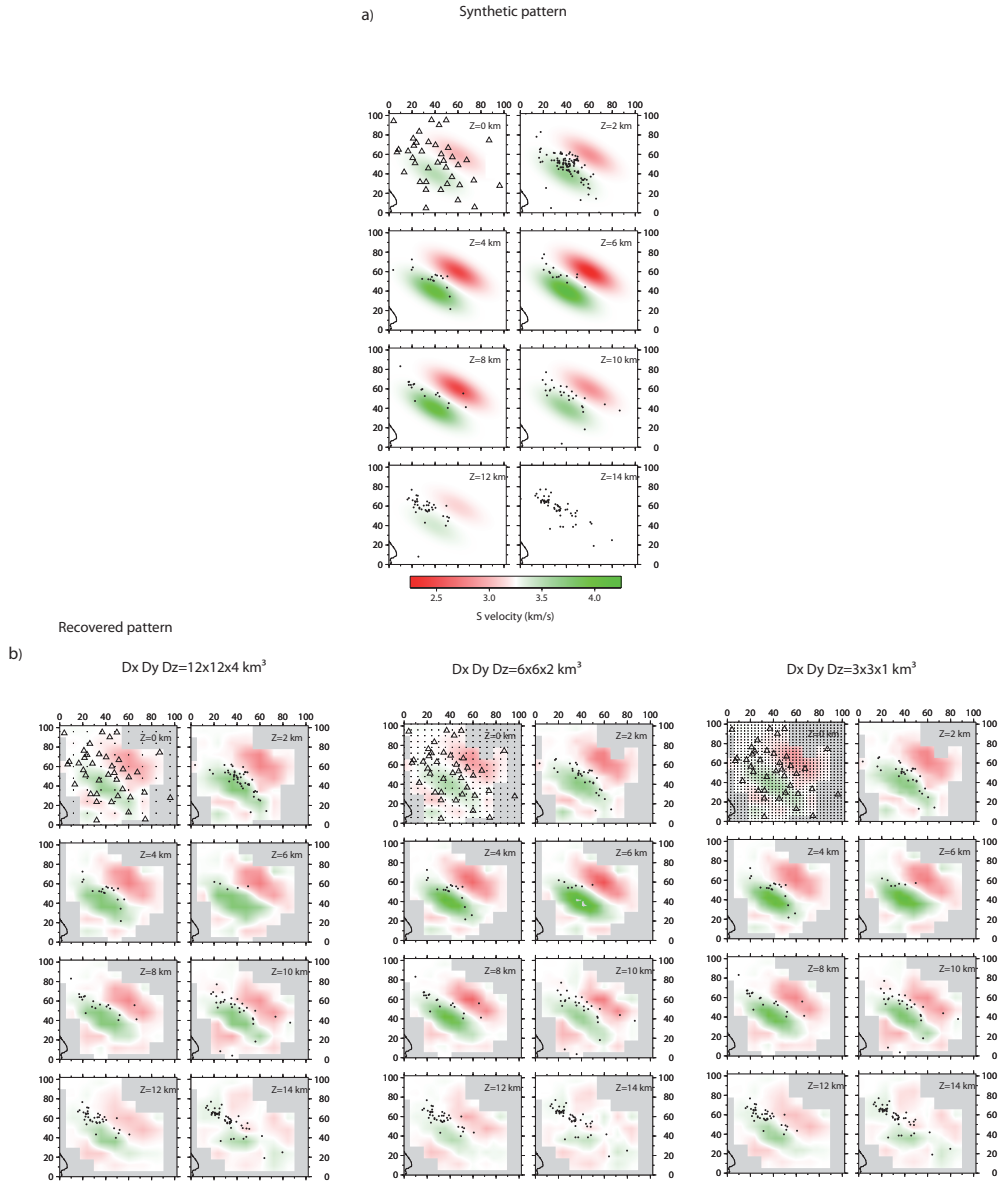
Figure 3.7: Multiscale approach: synthetic test for S velocity model. a) Synthetic pattern. b) Recovered pattern.
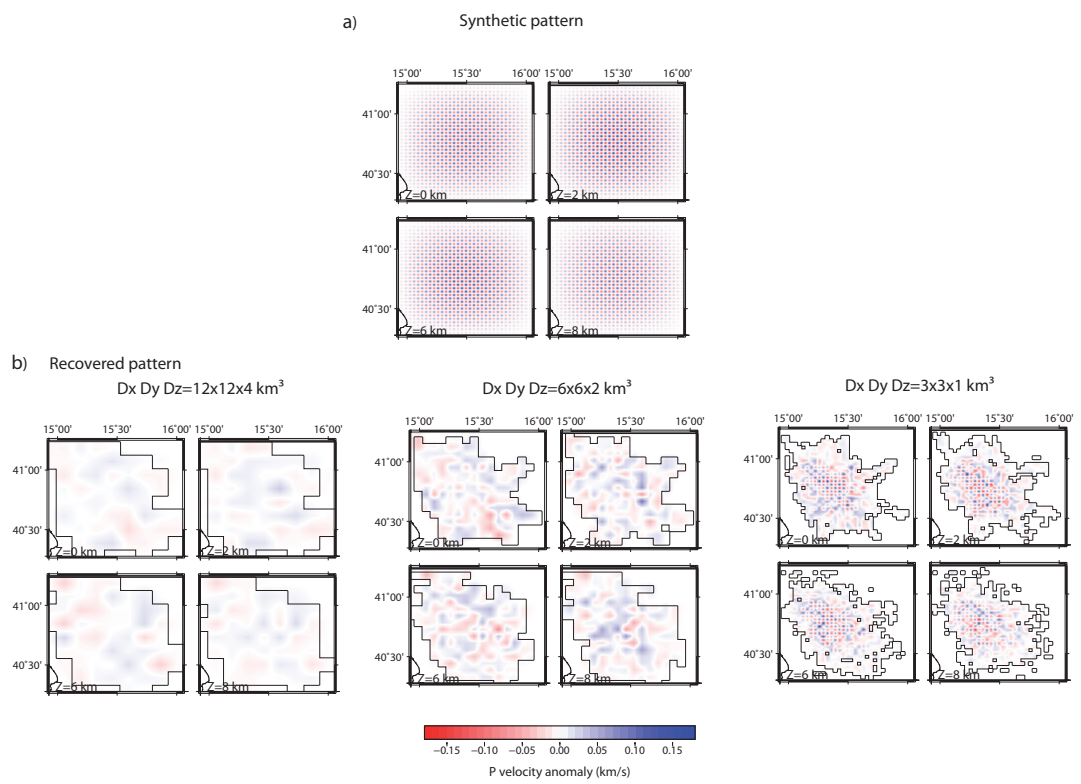
Figure 3.8: Multiscale approach: synthetic test.

tions must be large enough to yield traveltime perturbations above the noise level. Firstly, synthetic traveltimes are calculated for the real source-receiver geometry, secondly, these data are inverted using the background model of the anomaly pattern as the starting model and the same method as for the real experiment.

For each point of the nal model, the recovered anomaly pattern indicates the ability to resolve features with a length scale equal to the anomaly spacing. The semblance between exact and recovered checkerboard anomalies (*resolvability*) provides a quantitative estimate for the resolution. The resolvability r at a node is equal to

$$r = \frac{\sum_{i=1}^{N}(\Delta v_{t_i} + \Delta v_{r_j})^2}{\sum_{i=1}^{N}(\Delta v_{t_i}^2 + \Delta v_{r_j}^2)} \qquad (3.14)$$

where Δv_{t_i} and Δv_{r_i} are the true and recovered velocity anomalies at ith node. A qualitative indicator of the quality of the tomographic results are the ray coverage. In particular total ray length represents the accumulated ray length per cell sampled by wave arrival time dataset.

Chapter 4

Three dimensional P- and S-velocity models and earthquake locations

This section describes the application of the tomographic inversion of first arrival travel-times to determine the three-dimensional P and S velocity structure of the the Campania-Lucania region in the southern Apennines .

4.1   Gridding scheme and inversion strategy

The 3D P- and S-wave velocity models and earthquake locations have been obtained by inverting the dataset described in Chapter 2. Following the multiscale approach, explained in Section 3.5.2, the complete procedure consisted of three different inversions of 15 iterations in which the grid spacing is progressively decreased. Specifically, the used parametrizations are $12x12x4km^3$, $6x6x2km^3$ and $3x3x1km^3$. In order to analyse the effectiveness of the multiscale approach, it is worthwhile to look at the RMS reduction when moving from a coarse parametrization to a finer one. As shown in Figure 4.1 , it can be observed that starting from a value of 0.32s corresponding to the $12x12x4km^3$ parametrization, the RMS decreases to 0.14s in correspondence

of the 3x3x1km^3 parametrization with a total RMS reduction of 56%. The corresponding variations in the residuals distribution, defined as the difference between observed and computed travel-times, are shown in Figure 4.2. Although some outliers still remain, it can be noted that both the central value and the dispersion of the distributions largely improve with the decreasing of the space grid.

Before interpreting the final velocity models, for each of the selected parametrization, it is necessary to consider the ray coverage which is shown in Figure 4.3. In particular, panel (a) shows the map view of the grids while panels (b) and (c) show the P- and S-wave total ray length computed as the sum of the single ray lengths which cross the cell. Due to the relative sources-to-stations geometry, it can be noted that outer parts of the model are scarcely sampled by the rays. As a consequence, it is expected that these parts will be poorly resolved. On the other hand, due to the earthquakes location and stations density, the inner part of the model which is the main focus of the present Thesis, is expected to be better resolved. As a consequence of the adopted definition of the total ray length, it can be noted that the number of cells with higher total length values decreases with the increasing of the grid-spacing. The comparison among the two models allows to identify for the S-wave model a smaller covered region compared with the P-wave model at all the sampled depths. This can attributed to a total smaller number of S-phase readings.

Concerning the details of the inversion, the starting velocity model for the first parametrization corresponds to the 1D model optimized for the area and described in section 3.5.1. On the other hand, the multiscale approach requires that for subsequent parametrizations, the starting model corresponds to the final model of the previous parametrization. Moreover, the final model corresponds to the velocity values at each grid node.
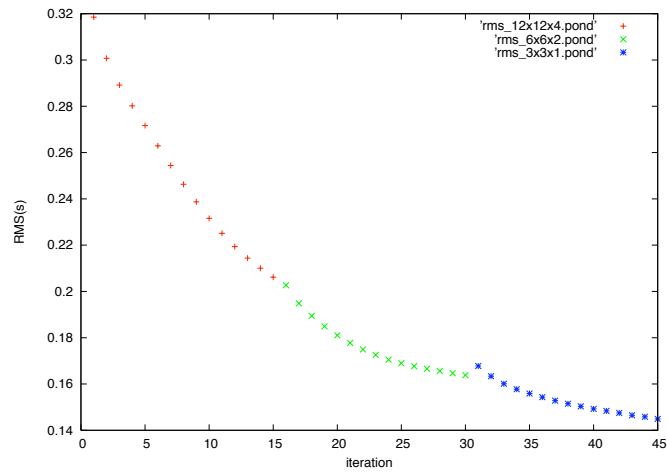
Figure 4.1:   RMS *vs* iteration number.   Red dots represent the RMS value obtained inverting P- and S-wave travel time using the first parametrization, green dots correspond to the second and third parametrization respectively.
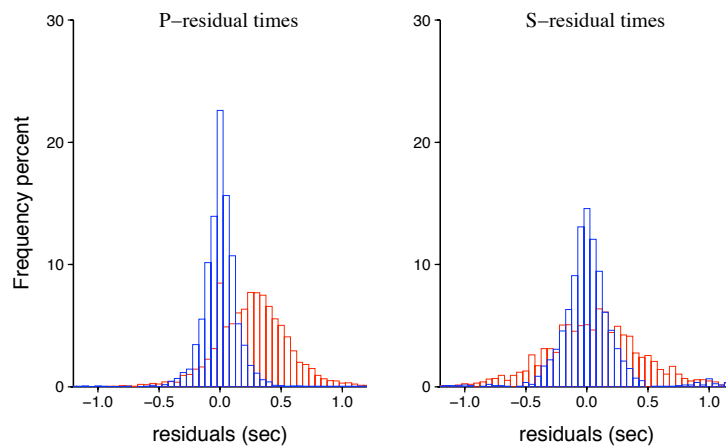
Figure 4.2:   Initial (red) and final (blue) distributions of travel-time residuals for P-wave and S-wave velocity models.

Figure 4.3:   Ray coverage. (a) Station-event distribution and grid spacing. (b) Map view of P total ray length. (c) Map view of S total ray length.

4.2 Results

4.2.1 Velocity models and earthquakes location

The final result of the inversion is a 3D model which is represented through slices at several depths and cross-sections. In particular, according to the results shown in Figure 4.3 the selected depths are: 0.0km, 4km, 8km and 12 km. Figures 4.4 and 4.5 show a map view of P- and S-wave velocity models for each of the selected parametrizations at each of the selected dep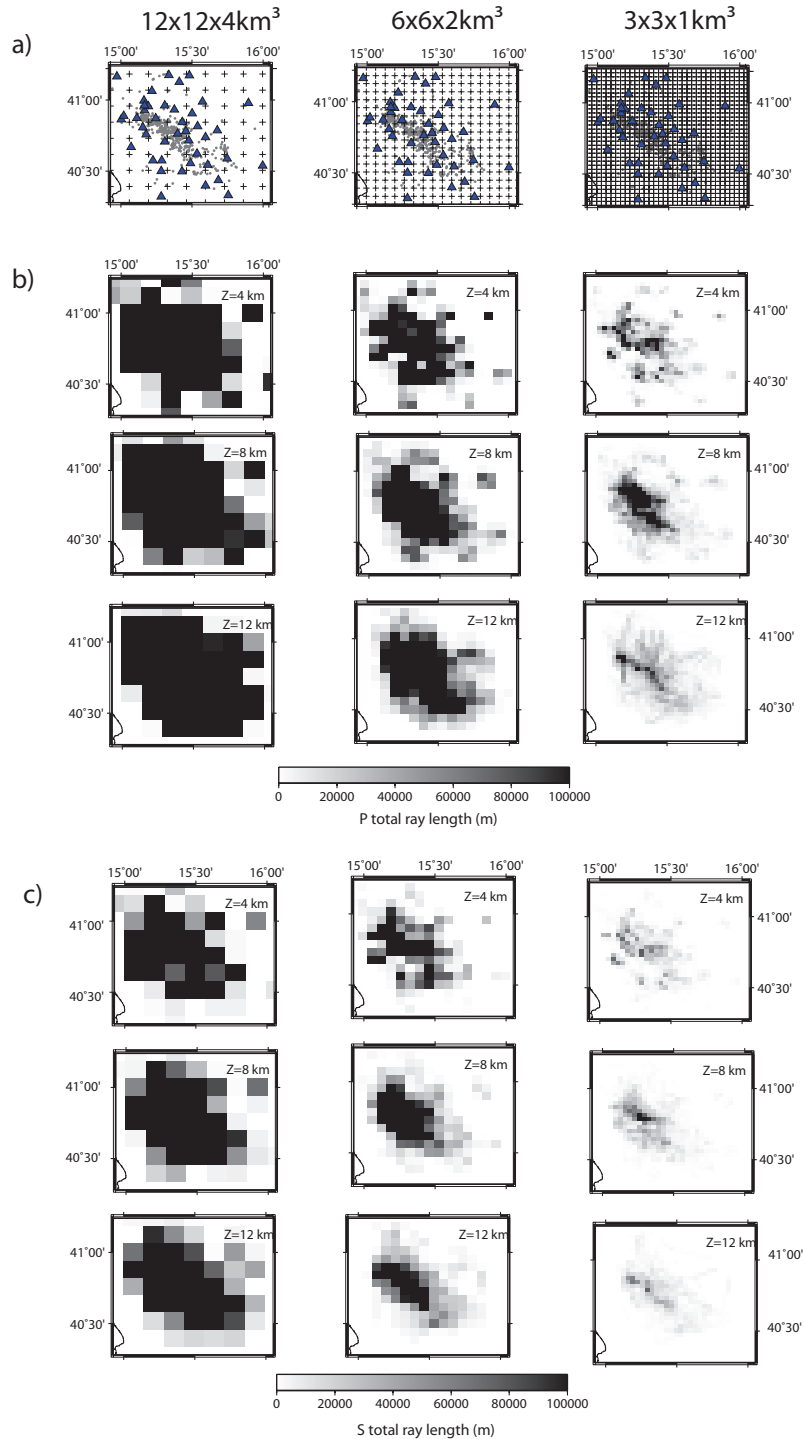ths. The stations distribution is shown in the layer correspondent to 0 km depth while black dots in all the panels indicate the earthquakes location. The regions not covered by the ray paths are shown in grey. The contour line corresponds to the 0.7 resolvability value is placed on each map. The P-wave model (Figure 4.4) indicates the presence of a strong velocity variation along a direction orthogonal to the Apenninic chain (i.e., anti-Apenninic), from 4 through 8 km depth. This variation defines two domains which are characterized by a relatively low (3.5 - 4.8 km/s) and high (5.2- 6.5 km/s) velocity, respectively. This characteristic is not longer evident in the deeper part of the model. The S-wave velocity model (Figure 4.5) shows a velocity change along the anti-Apenninic chain direction. However, the changes in the S-wave velocity values are weaker then the P-wave velocity values. In particular, at 8 km depth it is evident the presence of a relatively low velocity anomaly of 2.7 km/s located in south-east part of the model while a relatively high velocity anomaly (3.5-3.7 km/s) is found in the north-east part.

Additional information about the mechanic and physic properties of the rocks in the study are can be inferred from the analysis of the V_P/V_S ratio. In fact, as shown by several authors among which DeMatteis et al. (2008) and Chiarabba et al. (2009), the V_P/V_S ratio provides insights into effective stress, pore pressure, and sediment consolidation. In particular, a large consensus does exist about the correspondence between large values of the ratio indicate and the presence of fluids. However, as indicated by Trippetta et al. (2010), both laboratory data and tomographic analyses show that significant varia-

tions are expected for an already fully saturated rock mass wit respect to dry
rock. The map of the V_P/V_S ratio deduced for the area under study is shown
in Figure 4.6. From 0 km to 4 km depth the model is dominated by a ratio
value lower than 1.8. At 8 km depth the ratio values increases showing values
higher than 1.9 which are mainly located in the south-west part of the model.
Additionally, the V_P/V_S ratio maps allow also to recognize that the area char-
acterized by the values observed at 8 km depth takes a slightly different form
in the second parametrization with respect to the other parametrizations. It
is worthnoting that this feature could not have been inferred from the analysis
of the single models separately.

Based on the results discussed so far, we deduced that the second parametriza-
tion is sufficient for a reasonable imaging of the velocity anomalies. This is
particularly evident when the velocity contrast observed in the anti-Apenninic
direction (Figure 4.4) is referred to. As a consequence, in the remaining part of
the section, only the model obtained by using this parametrization $6x6x2km^3$
will be discussed.

As stated above, a complete visualization of a 3D model requires that also
cross-section should be visualized and interpreted. To this aim, Figure 4.7
shows three different sections corresponding to the profiles reported in panel
(a) of the same figure. It can be observed that the velocity variations are more
important moving from northwest to southeast. The seismicity intercepted by
the profiles AA' and and BB' is more concentrated at depth larger than 10
km. On the other hand, the seismicity related to the CC' profile shows a cloud
distribution which does not allow to identify any particular alignment.

As a final analysis, the cross-sections showing the percentage variations of the
final models with respect to the initial models have been produced. These
sections provide an additional support for interpreting the V_P/V_S ratio be-
cause they help in discriminating if a variation in the ratio has to be mainly
attributed to a variation in the V_P values or in the V_S values. As a general
observation, for all the considered cross-sections, the percentage values range
between ±25%. On the other hand, the section of the deduced V_P/V_S ratio

shows that the ratio is lower than 1.8 in the shallow part, while for depths ranging between 5 km and 12 km the ratio increases up to 2.1 in correspondence to the area of higher seismicity. This confirms that areas characterized by higher values are much more prone to generate earthquakes as a response to the presence of fluids and higher pore-pressures.

4.2.2   Resolution analysis

To evaluate the spatial resolution of the inferred 3D models, a checkerboard test was performed. The checkerboard has been generated by using a sinusoidal function having a wavelength corresponding the grid spacing and an amplitude of 0.18 km/s. In practice the checkerboard was added to the starting tomographic models and the travel-times, computed fixing the earthquake locations, were inverted for both P- and S-wave velocity models.
The assessment of the recovered anomaly patterns was estimated through the *resolvability* function reported in equation 3.14.

4.2.3   Comparison with previous studies

In order to give a geological interpretation to the inferred velocity values, a comparison with a portion of the structural section obtained interpreting the profile CROP04 (Cippitelli, 2007) has been made. In particular, the western and axial sectors have been selected and the corresponding P-wave velocity model has been overlapped. The result is shown in Figure 4.10 where the main seismic reflectors, the top of the Apennine Platform, the top of Lagonegreo-Irpina flysch sequence or imbricate, the top Apulian Platform and the base of the carbonate sequence, can be identified. In correspondence of the San Gregorio Magno well the uplift of the Apulian Platform is observed up to 5km depth overlaid by Lagonegro-Irpinia flysch units. The part between the San Gregorio Magno well and San Fele well contains several normal faults cutting the accreationary wedge (Cippitelli, 2007). In particular, the fault outcropping at the Piano delle Pecore on Mt Marzano, has been recognized as the fault on
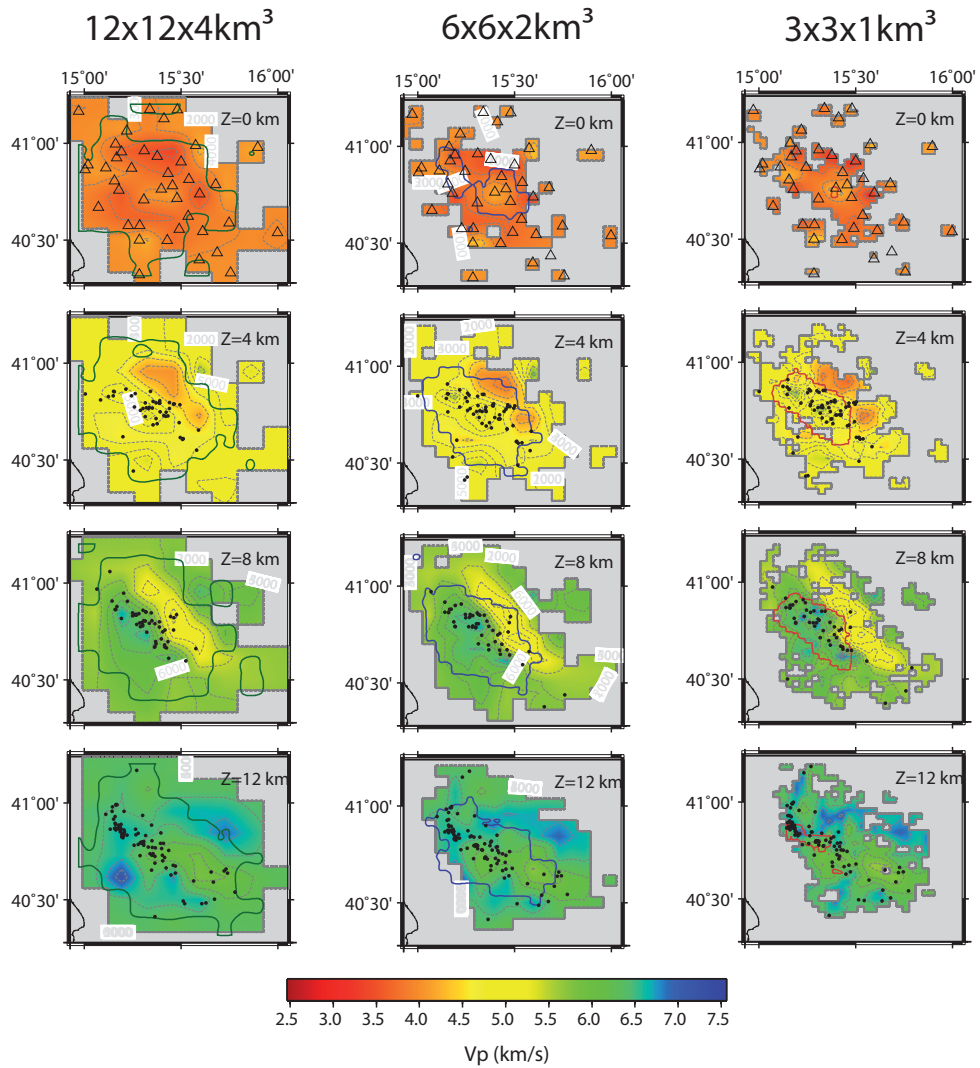
Figure 4.4:   Map view of Vp velocity models at each parametrization.
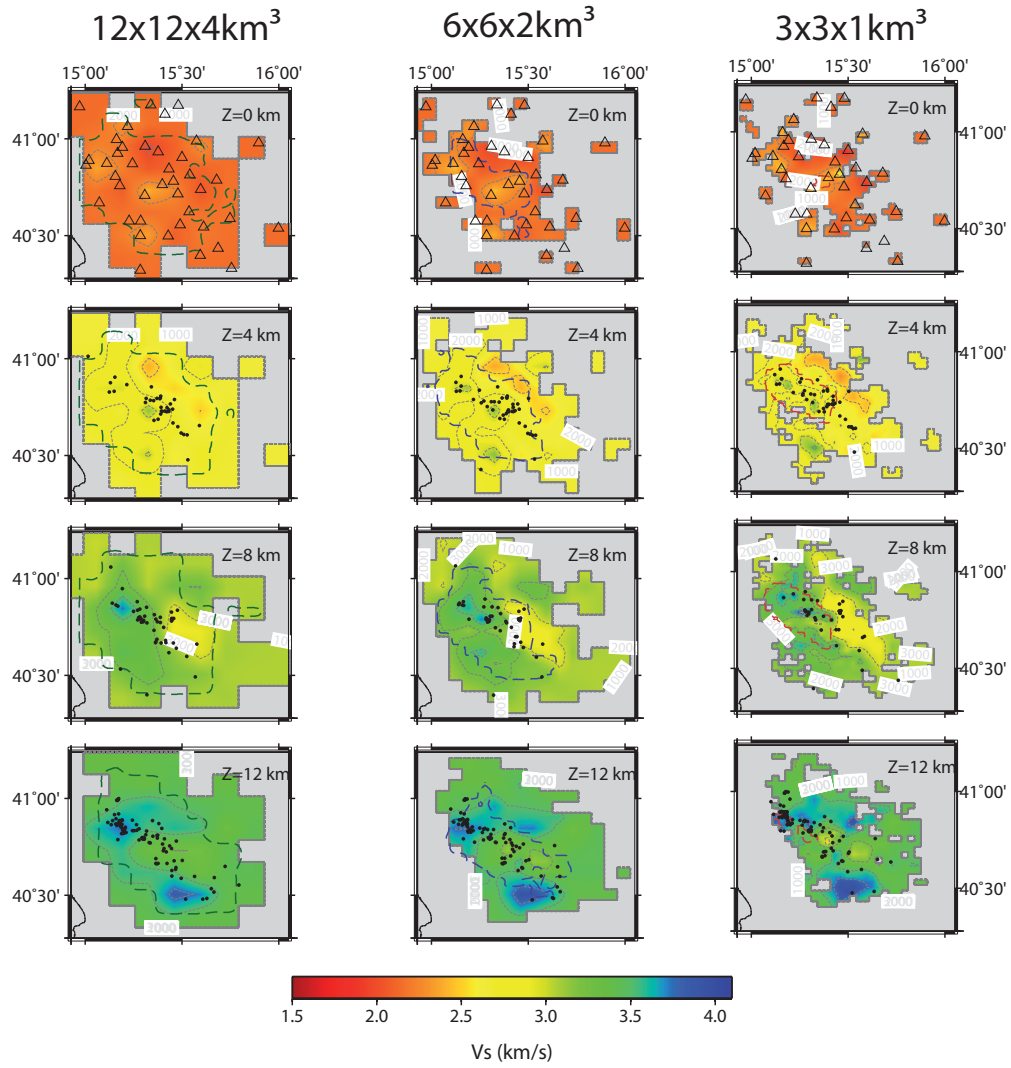
Figure 4.5:   Map view of Vs velocity models at each parametrization.
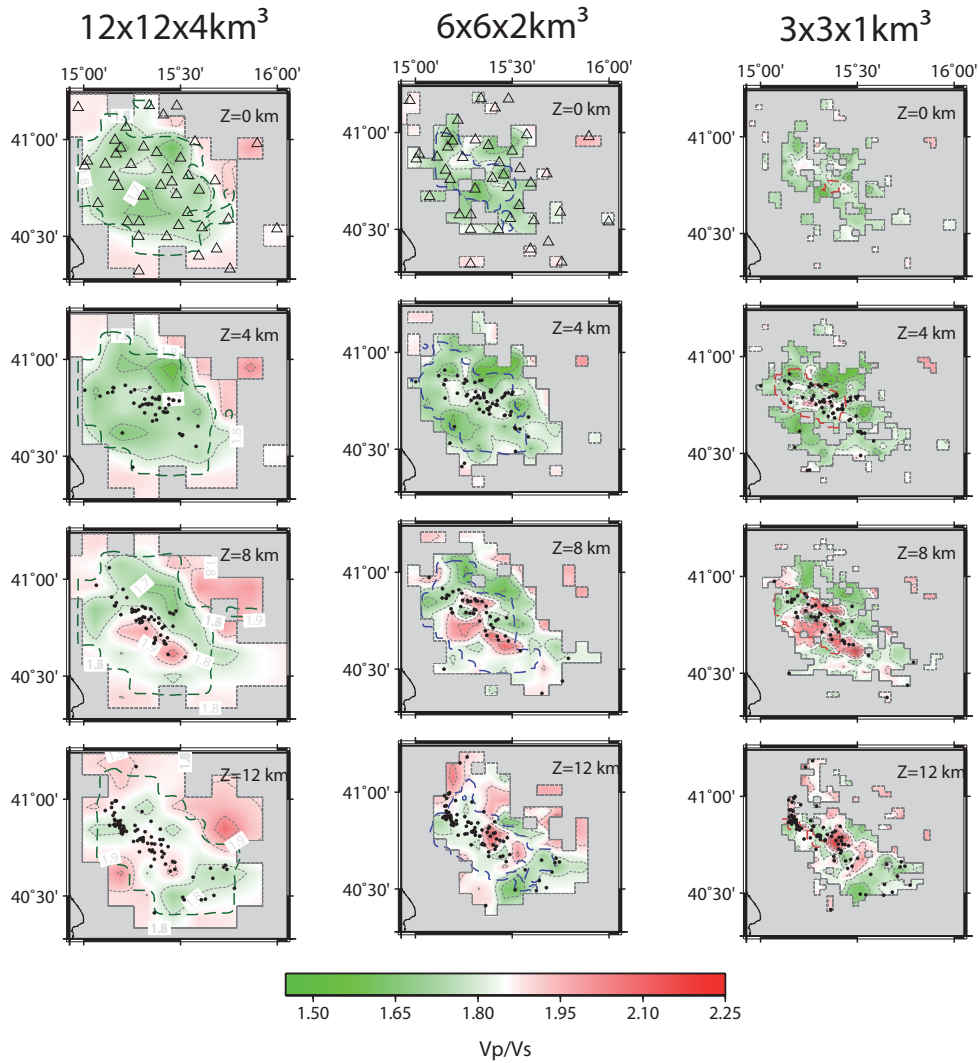
Figure 4.6: Map view of Vp/Vs velocity models at each parametrization.
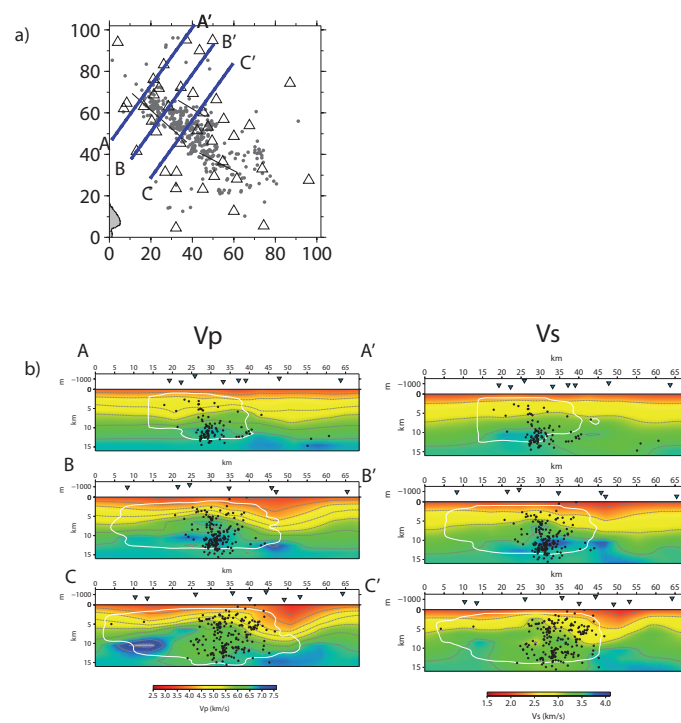
Figure 4.7:   (a) Map show hypocentral location.   (b) Anti-Apenninic sections showing V_P and V_S . The well-solved area is contoured by withe line.
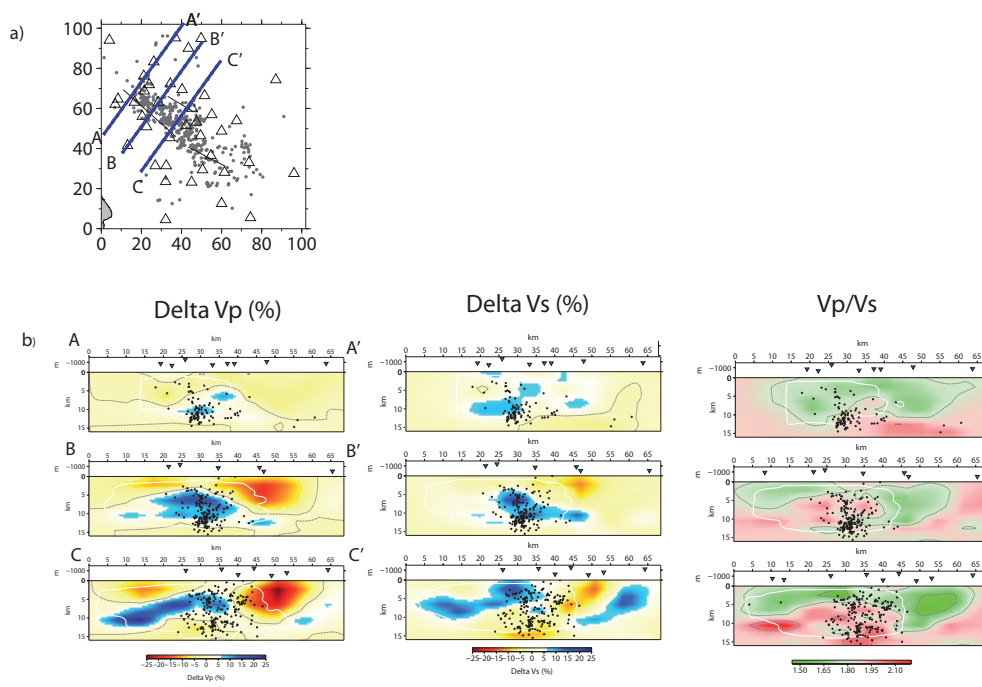
Figure 4.8: (a) Map showing earthquakes hypocentral location. (b) Anti-Apenninic sections showing δV_P δV_S and V_P/V_S. Velocity variations are expressed in percentage with respect to the starting model. The well-solved area is contoured by a white line.
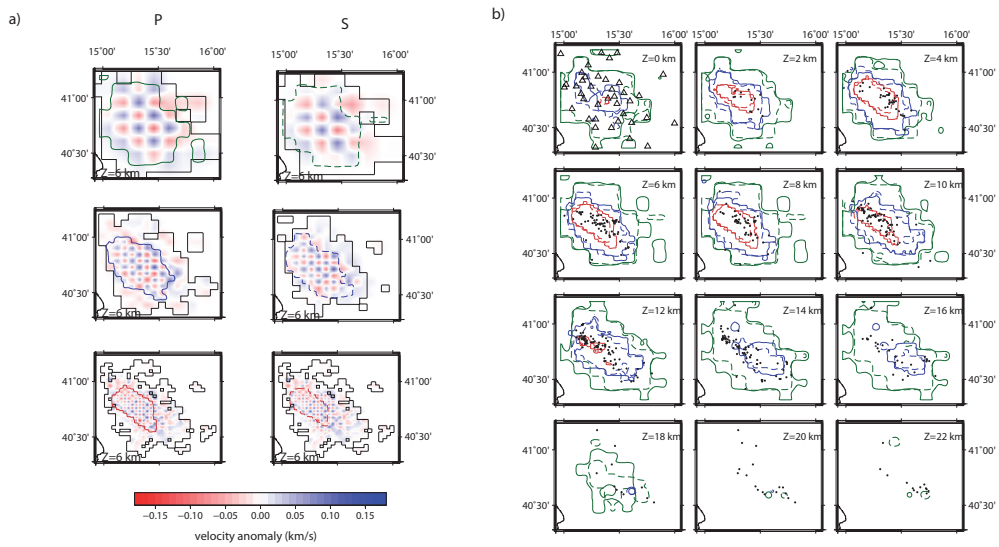
Figure 4.9: Resolvability of checkerboards. (a) Example of recovered anomaly patter from a synthetic checkerboard test for both P- and S-wave velocity models at 6 km depth. The coloured solid contour line corresponds to r=0.7 for the P-wave velocity model having parametrization 12x12x4km^3 (green line), 6x6x2km^3 (blue line) and 3x3x1km^3 (red line). The coloured dashed contour line corresponds to r=0.7 for the S-wave velocity model having parametrization 12x12x4km^3 (green line), 6x6x2km^3 (blue line) and 3x3x1km^3 (red line). (b) Resolvability of 0.7 calculated for the P-wave and S-wave velocity models.

which the 1980 Irpinia earthquake nucleated (Pantosti and Valensise, 2001). The analysis of panel (b) in Figure 4.10 shows that the inferred velocity model reproduces the main geological features identified in the CROP04 profile. Specifically, the uplift of the Apulian carbonate Platform is well identified by the high-velocity anomaly whose value ranges between 6.0-6.8 km/s in agreement with the values obtained by (Improta et al., 2003). The thickening of the Lagonegreo units located in the axial sector are well reproduced by the low velocity values ranging between 4.0-4.5km/s whose east-worth extension is identified by the lower velocity values just above the Apulian Platform in the depth range between 4.0 and 8.0 km. However, the poor resolution of the shallower layers does not allow to identify the Apenninic carbonate Platform whose velocity values range between 5.3 and 6.0km/s. Panel (c) of Figure 4.10 shows the 1D velocity profiles extracted from the velocity model in correspondence of the Contursi, San Gregorio Magno and San Fele wells which are indicated in the upper panel of the same figure. The profiles corresponding to Contursi and San Gregorio Magno wells indicate that the P-wave velocity linearly increase with the depth reaching a maximum value of about 7 km/s at a depth of about 6 km. Additionally, concerning the San Gregorio Magno profiles a decrease of the velocity values can be noted starting from depth larger than 8 km which reproduce the thickness of the Apulian carbonate Platform in correspondence of the well. The profile corresponding to the San Fele well features a slower velocity gradient as function of the depth.

The joint inversion of both earthquakes location and velocity models allows to infer information about the analyzed seismicity distribution. Seismicty map view is shown in panel (a) of Figure 4.10 together with the stations distribution. Two main features can be discriminated from the analysis of the seismicity. Specifically, the seismicity located in the northern part of the region is mainly characterized by a north-west south-east elongation covering the area embedding the faults system on which the 1980 Irpinia earthquake originated (Figure 1.5). The seismicity located in the southernmost part of the map is characterized by an east-west trend which can be linked with the faults on which the

1990 Potenza earthquake and the 1991 Potenza earthquake originated characterized by strike-slip mechanisms. The depth distribution of the seismicity shown in panel (b) of Figure 4.10 reproduce the cloud distribution observed in the cross-sections shown in 4.7. This result is compatible with the observation that earthquakes in the area occur on a graben-like structure characterized by a sequence of several trending sub-parallel faults (De Matteis et al, 2012).
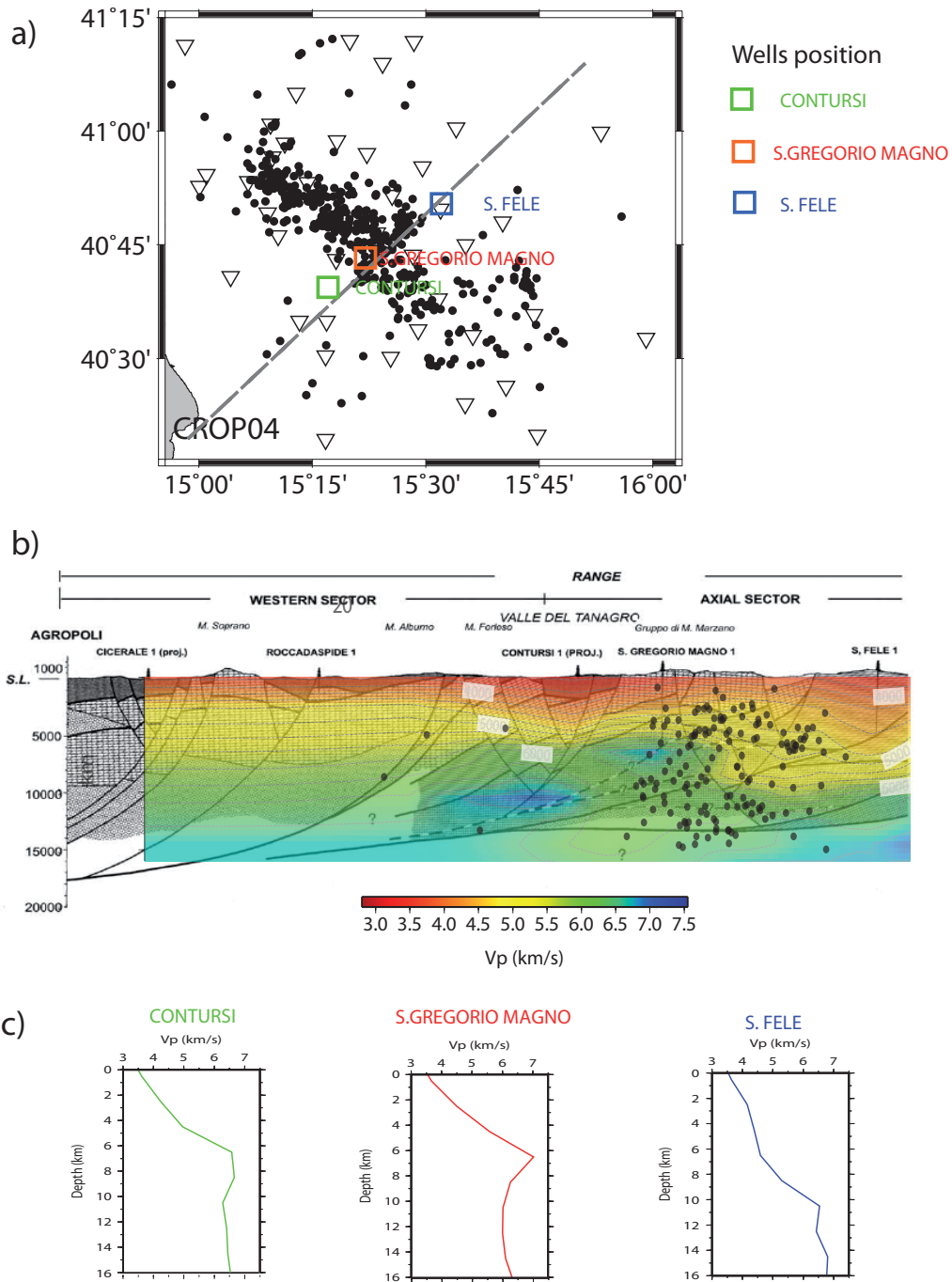
Figure 4.10: Results interpretation. (a) Map view of seismicity. (b) Comparison between the inferred P-wave velocity model and structural section obtained interpreting the profile CROP04 (Cippitelli, 2007). (c) 1D Vp velocity profile extracted in correspondence of the Contursi, San Gregorio Magno and San Fele wells.

Appendix A

Physical interpretation of station static correction

The station correction are integral part of the minimum Minimum 1D model obtained using the technique of Kissling et al. (1994). How they are distribuited is very important for our understanding of seismic images.

A.1 Evidence of static correction

The distribution of station corrections shows a strong lateral variation in the anti-Apenninic direction, which is consistent with the transition between the carbonatic platform outcrops at South-West and the Miocene sedimentary basins at North-East (Matrullo, Amoroso, Matteis, Satriano, and Zollo, Matrullo et al.). The comparison of the station corrections distribution with the top of the Apula Carbonate Platform and the entity of the retreived station corrections highlights that these station delays are clear indicators of strong lateral velocity variations in the near-surface but also likely throughout the crust (Figure A.1).
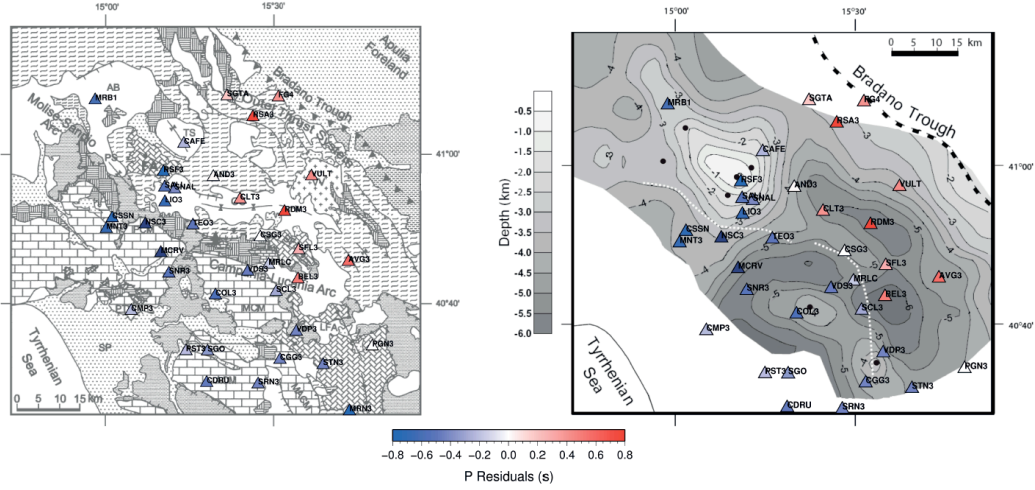
Figure A.1: Spatial distribution of station correction (Matrullo, Amoroso, Matteis, Satriano, and Zollo, Matrullo et al.). (a) Comparison with geological map proposed by Improta et al., 2003 (a) Comparison with contour map of the top of the Apulia Carbonate Platform proposed by Improta et al. (2003)

A.2   P-wave tomography

In order to interpret the observed station corrections pattern a three-dimensional crustal velocity model has been obtained from the tomographic inversion of the same data set of P first-arrival. The inversion is performed using an improved method based on an accurate finite-difference traveltime computation and a simultaneous inversion of both velocity models and earthquake locations (see Chapter 3). To solve the inverse problem related to the non linear relation we follow an iterative scheme by which a linearized delay traveltime inversion is performed. First arrival travel times of wave fronts are computed through a finite difference solution of the eikonal equation (Podvin and Lecomte (1991)) in a fine grid of 0.5 x 0.5 x 0.5 km^3. The latter consists of constant slowness cells computed by trilinear interpolation from the inversion grid. For each event-receiver pair, travel times are recalculated by numerical integration of the slowness field along the previously traced rays (Latorre et al. 2004). Simultaneously, for each node of the inversion grid, travel time partial derivatives are computed for P slowness field, hypocenter location and origin time.

The parameters are inverted using the LSQR method of Paige and Saunders (1982). The iteration limit is set to 5000 internal iteration while the number of inversion step is set up to a maximum of 20 iterations. The control of the model roughness is achieved by the requirement that the Laplacian of the slowness file must vanish during the inversion procedure (Benz et al. 1996, Menke 1984). The mistfit function, defined as the sum of the squared time delay, is a posteriori analysed and the convergence is usually reached after 10 or 15 iterations. We used a nodal representation, in which velocity field is reconstructed by three-dimensional grid. In this way we dont́ introduce a specific geometry of heterogeneities. Different grid spacing are tested and in particular we performed several inversions progressively decreasing the distance of each node corresponding at increasing of the number of parameters. We choose the optimal parametrization according to the minimum of the Akaike Information Criteria (AIC) (Akaike, 1974). The minimum was obtained for the model with 6x6x2 km^3 grid spacing (Table A.1). We performed the inversion starting from

Grid Spacing (km^3)	RMS(s)	AIC
24x2x8	0.165	-13386
12x12x4	0.135	-14900
6x6x2	0.105	-15398
3x3x1	0.086	-8759
1.5x1.5x0.5	0.075	19063

Table A.1: Estimate AIC for different model parametrizations.

the best 1D Minimum velocity model. The obtained model, with the associated static delay time for each station, are re-inverted to find the final model. The station corrections computed in 3D velocity model become very close to zero, indicating that the inversion procedure converges (Tables A.2 A.3). The obtained a RMS reduction is about 68% with a final value of 0.1 s.

The tomographic image clearly indicates the presence of a strong velocity variation along the direction orthogonal to the Apenninic chain, from 5 to 8-9

Station	Corr 1D	Corr 3D
AND3	0.0204	0.0
AVG3	0.5730	-0.0565
BEL3	0.4973	-0.0184
CGG3	-0.4299	-0.0144
CLT3	0.3978	-0.0009
CMP3	-0.2309	-0.011
COL3	-0.5693	-0.0011
CSG3	0.0	0.0207
LIO3	-0.6667	0.0246
MNT3	-0.6662	0.011
NSC3	-0.9273	-0.0313
PGN3	0.0002	-0.0235
PST3	-0.2245	-0.1055
RDM3	0.9312	-0.0219
RSA3	0.8284	-0.1346
RSF3	-0.7930	-0.0460
SCL3	-0.2876	0.0208
SFL3	-0.5275	-0.0240
SNR3	-0.4424	-0.0243
SRN3	-0.4359	-0.0204
STN3	-0.5039	-0.0488
TEO3	-0.4318	-0.0258
VDP3	-0.4735	-0.0376
VDS3	-0.236	-0.0127
CAFE	-0.4850	-0.0235

Table A.2: Station corrections in 1D and 3D velocity models.

Station	Corr 1D	Corr 3D
CDRU	-0.2691	-0.013
CMPR	-0.6982	0.0070
CSSN	0.4003	-0.0188
FG4	-0.7665	-0.0325
MCEL	-0.8069	0.0021
MCRV	-0.6055	-0.0042
MRB1	-0.1658	-0.0877
MRLC	1.0332	-0.0062
PALZ	0.3268	-0.0046
PTRP	-0.3537	-0.0050
SGO	0.1805	0.0024
SGTA	-0.3221	-0.0230
SNAL	-0.4138	-0.0150
VULT	0.4505	0.0087
MRN3	-0.7777	0.0012
SALI	-0.5160	-0.0656
SLCN	-0.3221	0.032554

Table A.3: Station corrections in 1D and 3D velocity models.

km of the crust, defining two domains characterized by relatively low (3.5 - 4.8 km/s) and high (5.2 - 6.5km/s) velocity respectively (Fig.6a). To verify the spatial resolution of the inferred 3-D model, standard checkerboard test were performed. We add a small anomaly pattern to grid node values of our final velocity models in order to keep the same ray coverage. In Fig.6 we display the synthetic and the recovered pattern. Resolved anomalies are located between 4 and 15 km depth. The anomaly pattern is not recovered at the surface and for depth grater than 15 km. However lateral smearing is detected where ray distribution in not able to reconstruct small features. The comparison of retrieved Vp anomalies with the spatial distribution of 1D derived station corrections confirms that the latter reflects the large-scale geological changes.
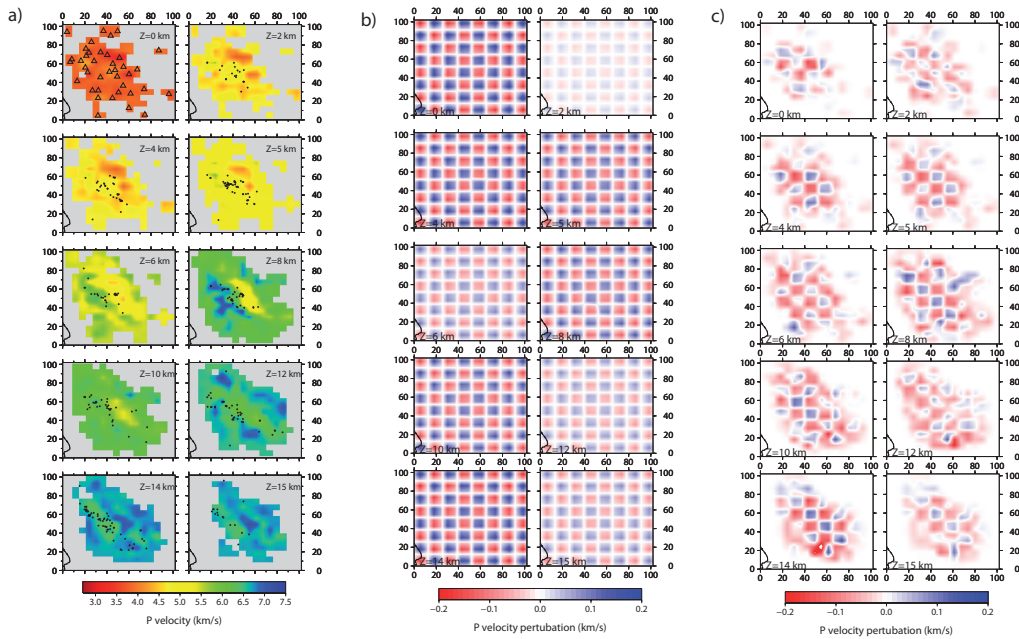

Figure A.2:   Final tomographic model of P velocities and checkerboard test. (a) Map view show velocity layers between 0 and 15 km depth, the regions that are not covered by the ray paths have been masked in grey. (b) Synthetic pattern added to the 3D final tomographic model. (c) Map view at different depth of the recovered pattern.

A.3 Interpretation

The 3D P-wave velocity model provides a physical explanation of the station corrections distribution and confirm that the station corrections reflect lateral variations of P-wave velocity at great depths. A good agreement on the large scale between the tomographic sections and the geological sections obtained from the interpretation of other geophysical data was obtained. The 3D Vp images show that the crust is characterized by a complex tectonic pattern: the high velocity body can be correlated with the Apenninic and the Apulia carbonatic platforms whereas the low velocity bodies can be associated to the basinal deposits. The velocity ranges associated to the main geological units of the area are compatible with previous study in the area. The tomographic result clearly indicates the presence of a strong velocity variation along the direction orthogonal to the Apenninic chain, with anomalies correlated the carbonatic platform outcrops at South-West and the sedimentary basins at North-East consistent with the margin of the Western Carbonate Platform. It should be emphasized that the NE rather deep sedimentary basins are clearly visible which dominate the velocity values considerably

Conclusions

The purpose of the present Thesis was to infer a three dimensional image of the faults system in Southern Apennines of Italy on which the last destructive 23 November 1980 M 6.9 earthquake occurred. The analysis was carried on by jointly interpreting both P- and S-waves velocity models and re-locating the background seismicity recorded by the Irpinia Seimic Network (ISNet) and some stations from the national network managed by the Istituto Nazionale di Geofisica e Vulcanologia (INGV).

In order to achieve promising results both the problem of data quality and the selection of a reliable and robust inversion strategy have been faced. The Thesis has been thus developed along two main lines. The first part has been devoted to develop optimized procedures for the measurements of P- and S-wave arrival times, through the use of polarization filtering and to the application of a refined re-picking technique based on cross-correlation of waveforms. The second problem was faced by adopting a technique of iterative tomographic inversion, linearized, damped combined with a strategy of multiscale inversion type.

The methodological approach aimed at an unequivocal identification of the S-wave arrival times is based on the integration of polarization analysis on single three-components recordings with the analysis and the estimation of lateral waveforms coherence through multichannel processing techniques applied to seismic sections.

In order to obtain highly accurate readings, the automatic refined re-picking technique proposed by Rowe et al (2002) has been used. The technique was

applied to both the P- and S-phase first arrival-times read manually and those obtained from the polarization analysis. The application of this technique produces a significant improvement when we look at the re-alignment of the waveforms with respect to the new estimated arrival-time.

Once solved the problem of P- and S-phase reading accuracy the problem of the determination of an accurate velocity model has been addressed . The code for the tomographic inversion used is TOMO_TV. It was developed during the thesis by Professor Jean Virieux from Joseph Fourier University in Grenoble, and adapted, implemented and tested in the present Thesis through a series of numerical tests on synthetic and real data. The software was also integrated with a package of procedures for calibrating the damping parameters and for studying the resolution of the retrieved tomographic images. Considering the real events-to-stations distribution, sensitivity analyses were performed, considering an ideal model, the initial and final velocity model to perform the correct tuning of the hyper-parameters, the damping parameter and the optimal velocity model parametrization. In particular, we adopted a multi-scale approach, which allows for the reconstruction of velocity anomalies with a scale length ranging from ten of kilometres down to less then on kilometre in correspondence of the central part of the investigated area.

As a main result, the retrieved P-wave velocity model indicates the presence of a strong velocity variation along a direction orthogonal to the Apenninic chain from 4 km through 8 km depth. This variation defines two domains which are characterized by a relatively low (3.5 - 4.8 km/s) and high (5.2- 6.5 km/s) velocity values. On the other hand, the S-wave velocity model shows a velocity change along the anti-Apenninic chain direction. However, the changes in the S-wave velocity values are weaker than the P-wave velocity values. The availability of both P- and S-wave velocity models allowed to investigate the V_P/V_S which has been proved to be related to the physical and mechanical properties of the rocks. The deduced V_P/V_S ratio shows that the ratio is lower than 1.8 in the shallower part of the model, while for depths ranging between 5 km and 12 km the ratio increases up to 2.1 in correspondence to the area of

higher seismicity. This confirms that areas characterized by higher values are more prone to generate earthquakes as a response to the presence of fluids and higher pore-pressures.

From the comparison between the inferred P-wave velocity model with a portion of the structural section obtained interpreting the profile CROP04 (Cippitelli, 2007) the uplift of the Apulian carbonate Platform is well identified by a high-velocity anomaly whose value ranges between 6.0-6.8 km/s in agreement with the values obtained by Improta et al, (2003). The thickening of the Lagonegreo units located in the axial sector are well reproduced by the low velocity values ranging between 4.0-4.5km/s whose east-worth extension is identified by the lower velocity values located above the Apulian Platform in the depth range between 4.0 and 8.0 km.

Concerning the re-located seismicity two main features can be discriminated. Specifically, the seismicity located in the northern part of the region is mainly characterized by a north-west south-east elongation covering the area embedding the faults system on which the 1980 Irpinia earthquake originated. The seismicity located in the southernmost part of the map is characterized by an east-west trend which can be associated the faults on which the 1990 Potenza earthquake and the 1991 Potenza earthquake originated which are characterized by strike-slip mechanisms. Moreover, the depth distribution of the seismicity is characterized by a cloud distribution. As noted in a recent study by De Matteis et al, (2012) this characteristic can be ascribed to the fact that the earthquakes located in the study area occur on a graben-like structure characterized by a sequence of several trending sub-parallel faults and not along a unique well define fault.

Bibliography

Akaike, H. (1974). A new look at the statistical model identification. *IEEE Trans. Autom. Control 6*, 716–723.

Aki, K. and W. Lee (1990). Determination of three-dimensional velocity anomalies under a seismic array using first p arrival times from local earthquakes, i, a jomogeneous initial model. *Journal Geophys. Res.*, 4381–99.

Allen, R. (1978). Automatic phase pickers: their present and furure prospects. *Bull. Seism. Soc. Am. 72*, S225–S242.

Amato, A., C. Charabba, L. Malagnini, and G. Selvaggi (1992). Three-dimensional p-velocity structure in the region of the ms=6.9 irpinia, italy, normal faulting earthquake. *Physics of the Earth and Planetary Interiors. Elsevier Scince B V, Amsterdam 75*, 111–119.

Amato, A. and P. Montone (1997). Present-day stress field and active tectonics in southern peninsular italy. *Geoph.J. Int. 130*, 519–534.

Amato, A. and G. Selvaggi (1993). Aftershock location and p-wave velocity structure in the epicentral region of the 1980 irpinia earthquake. *Ann. Geofis. 36*(1).

Amoroso, O., N. Maercklin, and A. Zollo (2012, April). S-wave identification by polarization filtering and waveform coherence analysis. *Bull. Seism. Soc. Am. 36*(102-2), 3–15.

Anzidei, M., P. Baldi, G. Casula, A. Galvani, E. Mantovani, A. Pesci, F. Riguzzi, and E. Serpelloni (2001). Insights into present-day crustal motion in the central mediterranean area from gps surveys. *Geoph.J. Int. 146*, 98–110.

Aster, R. and C. Rowe (2002, Jun). Automatic phase-pick refinement and similar event association in large seismic data sets. In *Advances in Seismic Event Location*, Volume 92, pp. 231–263. eds. C. Thurber and N. Rabinowitz. Kluwe, Amsterdam, 1993.

Battaglia, J., A. Zollo, J. Virieux, and D. D. Iacono (2008). Merging active and passive data sets in traveltime tomography: The case study of campi flegrei caldera (southern italy). *Geophys Prospect 56*(4), 555–573.

Benz, H., B. Chouet, P. Dawson, J. Lahr, R. Page, and J. Hole (1996). Three-dimensional p and s wave velocity structure of redoubt volcano, alaska. *J. Geophys. Res. 101*(B4), 8111–8128.

Bernard, P. and A. Zollo (1989, February). The irpinia (italy) 1980 earthquake: detailed analysis of complex normal faulting. *J. Geophys. Res. 94*(B2), 1631–1647.

Boncio, P., T. Mancini, G. Lavecchia, and G. Selvaggi (2007). Seismotectonics of strikeslip earthquakes within the deep crust of southern italy: Geometry, kinematics, stress field and crustal rheology of the potenza 19901991 seismic sequences (mmax 5.7). *Tectonophysics 445*, 281–300.

Bouchon, M. and K. Aki (1997). Discrete wave-number representation of seismic-source wave fields. *Bull. Seism. Soc. Am. 67*(2), 259–277.

Bunks, C., F. Saleck, S. Zaleski, and G. Chavent (1995). Multiscale seismic waveform inversion. *Geophysics. 60*, 335–341.

Casero, P., F. R. L. Endignoux, L. Moretti, C. Muller, L. Sage, and R. Vially (1991). Tectonic framework and petroleum potential of the southern apennines. *Oxford University Press, Oxford, UK 1*, 381–387.

Casnadei, R. (1998). Subsurface basin analysis of fault-controlled turbidite system in bradano trough, southern adriatic foredeep, italy. *Bull. Am. Assoc. Pet. Geol. 72*(11), 1370–1380.

Chatelain, J. (1978). *Etude fine de la sismicit en zone de collision continentale laide dun rseau de statios portables: la region Hindu-Kush-Pamir.* Thse de 3 me cycle, Univ. Paul Sabatier, Toulouse.

Chiarabba, C. and A. Amato (1994, December). From tomographic images to fault heterogeneities. *Annali di Geofisica 37*(6).

Chiarabba, C., D. Piccinini, and P. D. Gori (2009, Jan). Velocity and attenuation tomography of the umbria marche 1997 fault system: Evidence of a fluid-governed seismic sequence. *Tectonophysics 476*(1-2), 73–84.

Cichowicz, A. (1993). An automatic s-phase picker. *Bull. Seism. Soc. Am. 83*(1), 180–189.

Cippitelli, G. (2007). The crop-04 seismic profile. interpretation and structural setting of the agropoli-barletta geotraverse. *Boll.Soc.Geol.It. Ital.J.Geosci.* (TC3005), 267–281. Spec. Issue No. 7. (ed. by A. Mazzotti, E. Patacca and P. Scandone).

Cocco, M., C. Chiarabba, M. D. Bona, G. Selvaggi, L. Margheriti, A. Frepoli, F. Lucente, A. Basili, D. Jongmans, and M. Campillo (1999). The april 1996 irpinia seismic sequence: evididence for fault interaction. *J. Seism 3*, 105–117.

Cotton, F. and O. Coutant (1997). Dinamic stress variations due to shear faults in a plane-layered medium. *Geophys J. Int. 128*(3), 676–688.

Crampin, S. (1977). A review of the effects of anisotropic layering on the propagation of seismic waves. *Geophys J. R. ast. Soc. 49*, 9–27.

Dai, H. and C. MacBeth (1997). The application of back-propagation neural network to automatic picking seismic arrivals from single-component recording. *Journal of Geophysical Research* (102), 12105–15115.

DeMatteis, R., O. Amoroso, E. Matrullo, T. A. Stabile, L. A. Rivera, and A. Zollo (2011). Analysis of background microseismicity for crustal velocity model, fault delineation and regional stress direction in southern apennines, italy. *EOS Transactions, American Geophysical Union, Fall Meeting Supplement*.

DeMatteis, R., E. Matrullo, T. A. Stabile, L. A. Rivera, and A. Zollo (2012). Fault delineation and regional stress direction from the analysis of background microseismicity in southern apennines, italy. *Bull. Seism. Soc. Am..* under review.

DeMatteis, R., A. Romeo, G. Pasquale, G. Iannaccone, and A. Zollo (2010). 3d tomographic imaging of the southern apennines (italy): A statistical approach to estimate the model uncertainty and resolution. *Studia Geophysica et Geodaetica 54*(3), 367–387.

DeMatteis, R., T. Vanorio, A. Zollo, S. Ciuffi, A. Fiordelisi, and E. Spinelli (2008). Three-dimensional tomography and rock properties of the larderello-travale geothermal area, italy. *Physics of the Earth and Planetary Interiors 168*, 37–48.

Deschamps, A. and G. C. P. King (1984). Aftershocks of the campania-lucania (italy) earthquake of 23 november 1980. *Bull. Seism. Soc. Am. 74*, 2483–2517.

Diehl, T., N. Deichmann, E. Kissling, and S. Husen (2009). Automatic s-wave picker for local earthquake tomography. *Bulletin of the Seismological Society of America 99*(3), 1906.

DiLuccio, F., A. Piscini, N. A. Pino, and G. Ventura (2005). Reactivation of deep faults beneath southern apennines: evidence from the 19901991

potenza seismic sequences. *Terra Nova 17*, 586–590. doi: 10.1111/j.1365-3121.2005.00653.x.

Doglioni, C., P. Harabaglia, G. Martinelli, F. Mongelli, and G. Zito (1996). A geodynamic model of the southern apennines accretionary prism. *Terra Nova 8*, 540–547.

Eberhart-Phillips, D. (1986). Three-dimensional velocity structure in northern california coast ranges from inversion of local earthquake arrival times. *Bull. Seism. Soc. Am. 76*(4), 1025–1052.

Flinn, E. A. (1965). Signal analysis using rectilinearity and direction of particle motion. (53), 1874–1876.

Improta, L., M. Bonagura, P. Capuano, and G. Iannaccone (2003). An integrated geophysical investigation of the upper crust in the epicentral area of the 1980, ms= 6.9, irpinia earthquake (southern italy). *Tectonophysics 361*(1-2), 139–169.

Kanamori, H. (2005). Real-time seismology and earthquake damage mitigation. *Annu. Rev. Earth.*

Kanasewich, E. R. (1981). Time sequence analysis in geophysics. *The University of Alberta Press, Edmonton.*

Kissling, E., W. L. Ellsworth, D. Eberhart-Phillips, and U. Kradolfer (1994). Initial reference model in local earthquake tomography. *J. Geophys. Res*, 1–12.

Latorre, D., J. Virieux, T. Monfret, V. Monteiller, T. Vanorio, J.-L. Got, and H. Lyon-Caen (2004, Jan). A new seismic tomography of aigion area (gulf of corinth, greece) from the 1991 data set. *Geophys. J. Int. 159*, 1013–1031.

LeMeur, H., J. Virieux, and P. Podvin (1997). Seismic tomography of the gulf of corinth: A comparison of methods. *Ann. Geophys*, 1–25.

Lomax, A., C.Satriano, and M. Vassallo (2002, Jun). Automatic picker developments and optimization: Filterpicker - a robust broadband picker for real-time seismic monitoring and earthquake early-warning seismic monitoring and earthquake early warning. *Seismological Research Letters 92*, 1660–1674.

Lomax, A., J. Virieux, P. Volant, and B. Thierry (2000, Jun). Probabilis:tic earthquake location in 3d and layered models. in: Thurber c.h. and raibinowitz n. (eds.). *Advances in Seismic Event Location. Modern Approaches in Geophysics 18*, 101–134.

Lutter, W. J. and R. L. Nowack (1990, April). Inversion of the crustal structure using reflections from the passcal ouachita experiment. *Journal Geophys. Res.*, 4633–4646.

Lutter, W. J., R. L. Nowack, and L. Braile (1990, April). Seismic imaging of the upper crustal structure using travel times from the passcal ouachita experiment. *Journal Geophys. Res.*, 4621–4631.

Maggi, C., A. Frepoli, G. B. Cimini, R. Console, and M. Chiappini (2009). Recent seismicity and crustal stress field in the lucanian apennines and surrounding areas (southern italy): Seismotectonic implications. *Tectonophysics 463*, 130–144. doi:10.1016/j.tecto.2008.09.032.

Matrullo, E. (2012). *Fault delineation and stress orientation from the analysis of backgrounf, low magnitude seismicity in Southern Apennines (Italy)*. Phd thesis, Univ. of Bologna, Alma Mater Studiorum, Italy.

Matrullo, E., O. Amoroso, R. D. Matteis, C. Satriano, and A. Zollo. 1d versus 3d velocity models for earthquake locations: a case study in campania-lucania region (southern italy). In preparation.

Menardi, A. and G. Rea (2000). Deep structure of the campania lucanian arc (southern apennine, italy). *Tectonophysics 324*, 239–265.

Menke, W. (1989). *Geophysical Data Analysis: Discrete Inverse Theory.* Academic Press.

Michael, A. J. and D. Eberhart-Phillips (1991). Relation among fault behavior, subsurface geology, and three-dimensional velocity models. *Science*, 651–654.

Michelini, A. and A. Lomax (2004, Apr). The effect of velocity structure errors on double-difference earthquake location. *Geophys. Res. Lett.*, 1–4.

Montalbetti, J. F. and E. R. Kanasewich (1970). Enhancement of teleseismic body phases with a polariza-tion lter. *Geophys. J. R. Astr. Soc.*

Monteiller, V., J.-L. Got, J. Virieux, and P. Okubo (2005, Jan). An efficient algorithm for double-difference tomography and location in heterogeneous media, with an application to the kilauea volcano. *J. Geophys. Res. 110*(B12), 1–22.

Mostardini, F. and S. Merlini (1986). Appennino centro-meridionale. sezioni geologiche e proposta di modello strutturale. *Mem. Soc. Geol. Ital. 35*, 177–202.

Paige, C. and M. Saunders (1982). Lsqr: An algorithm fo sparse linear equation and sparse least squares. *ACM Transactions on Mathematical Software 8*(1), 43–71.

Pantosti, D. and G. Valensise (2001). Faulting mechanism and complexity of the 23 november, 1980, campania-lucania earthquake inferred from surface observations.

Pasquale, G., R. D. Matteis, A. Romeo, and R. Maresca (2009). Tectonic evolution of the outer margin of the apennines and related foredeep system. in: Boriani a., bonafede m., piccardo g.g. and vai g.b. *(Eds.) The Lithosphere in Italy: Advances in Earth Science Research 13*, 107–124. doi: 10.1007/s10950-008-9119-x.

Patacca, E. and P. Scandone (1987). Earthquake focal mechanisms and stress-inversion in the irpinia region (southern italy). *J. Seismol. 13*. Accademia Nazionale dei Lincei, Rome, Italy, 139-142.

Patacca, E. and P. Scandone (1989). Late thrust propagation and sedimentary response in the thrust belt foredeep system of the southern apennines (pliocene pleistocene). in: Vai, g.b., martini, i.p. (eds.), anatomy of an orogen: The apennines and adjacent mediterranean basins. *The Lithosphere in Italy 80*, 157–176. Accademia Nazionale dei Lincei, Rome, Italy, 139-142.

Patacca, E. and P. Scandone (2001). Late thrust propagation and sedimentary response in the thrust belt foredeep system of the southern apennines (pliocene pleistocene). *In: Vai, G.B., Martini,I.P. (Eds.), Anatomy of an Orogen: The Apennines and Adjacent Mediterranean Basins 45*, 401–440. Kluwer Academic Publishers, Dordrecht, Netherlands.

Patacca, E., P. Scandone, M. Ballatalla, N. Perilli, and U. Santini (1992). The numidian-sand event in the southern apennines. *Mem. Soc. Geol. Padova 13*, 297–337.

Pavlis, G. L. (1986). Appraising earthquake hypocenter location errors: a complete pratical approach for single-event locations. *Bull. Seism Soc. Am. 76*, 1699–1717.

Plesinger, A., M. Hellweg, and D. Seidel (1986). Interactive high resolution polarization analysis of boradband seismograms. *J. Geophys 59*, 129–139.

Podvin, P. and I. Lecomte (1991). Finite difference computation of travel-times in very constrasted velocity models: A massively parallel approach and its associated tool. *Geophys. J. Int*, 271–284.

Rost, S. and C. Thomas (2002). Array seismology: methods and applications. *Rev. Geophys 40*(3). doi:10.1029/2000RG000100.

Roure, F., P. Sasero, and R. Vially (1991). Growth processes and melange formation in the southern apennines accretionary wedge. *Earth Planet Sci. Lett. 102*.

Rowe, C., R. Aster, B. Brochers, and C. Young (2002, Jun). An automatic, adaptive algorithm for refining phase picks in large seismic data sets. *Bull. Seism. Soc. Am. 92*, 1660–1674.

Rowe, C., R. Aster, W. Phillips, R. Jones, B. Brochers, and M. Fehler (2002, Jun). Using automated, high-precision repicking to improve delineation of microseismicsstructures at soultz geothermal reservoit. *Pure appl. geophys 92*, 1660–1674.

Samson, J. C. (2002). Descriptions of the polarization states of vector processes: applications to ulf magnetic elds. *Geophys. J. R. Astr. Soc. (34(4))*, 403–419.

Scrocca, D., E. Carminati, and C. Doglioni (2005). Deep structure of the southern apennines, italy: Thinskinned or thickskinned? *Tectonics 24*(TC3005). doi:10.1029/2004TC001634.

Tarantola, A. and B. Valette (1987). Generalized nonlinear inverse problems solved using the least-squares criterion. *Rev. Geophys 20*, 219–232.

Thurber, C. (1992). Hypocenter-velocity structure coupling in local earthquqake tomography. *Phys. Earth Planet Inter*, 55–62.

Thurber, C. (1993). Local erathquake tomography: velocities and vp/vs - theory. *Chapman and Hall, London*, 563–583.

Thurber, C., S. Atre, and D. Eberhart-Phillips (1995). Three-dimensional vp and vp/vs structure at loma prieta, california from local earthquake tomography. *Geophys. Res. Lett 22*, 3079–3082.

Trippetta, F., C. Collettini, S. Vinciguerra, and P. Meredith (2010). Laboratory measurements of the physical properties of triassic evaporites from

central italy and correlation with geophysical data. *Tectonophysics 492*, 121–132.

Valensise, G. and D. Pantosti (2001). The investigation of potential earthquakes sources in peninsular italy: A review. *J. of Seismology 5*, 287–306.

Vanorio, T., J. Virieux, P. Capuano, and G. Russo (2005). Three-dimensional seismic tomography from p wave and s wave microearthquake travel times and rock physics characterization of the campi flegrei caldera. *J. Geophys. Res. 110*(B3).

Vassallo, M., C.Satriano, and A. Lomax (2002, Jun). Automatic picker developments and optimization: An optimization strategy for improving the performances of automatic phase picker. *Seismological Research Letters 92*, 1660–1674.

Vidale, J. E. (1986, October). Complex polarization analysis of particle motion. *76*(5), 1393–1405.

Waldhauser, F. and W. L. Ellsworth (2000, Dec). A double-difference eartquake location algorithm: Method and application to the northern hayward fault, california. *Bulletin of the Seismological Society of America*, 1–16.

Westaway, R. (1993). A geodynamic model of the southern apennines accretionary prism. *J. Geophys. Res 98*(21), 741–21,772.

Ylmaz, O. (1987). *Seismic data processing (Investigation in geophysics, vol 2)*. Society of Exploration Geophysicists, Tulsa, OK.

Zhang, H. and C. Thurber (2005, Mar). Adaptive mesh seismic tomography based on tetrahedral and voronoi diagrams: Application to parkfield, california. *J. Geophys. Res. 110*(B04303), 1–13.

Zollo, A., L. D'Auria, R. D. Matteis, A. Herreo, J. Virieux, and P. Gasparini (2002). Bayesian estimation of 2-d p-velocity models from active seismic

arrival time data: imaging of the shallow structure of mt vesuvius (southern italy). *Geophys. J. Int. 151*, 566–582.